ALMA MATER STUDIORUM
UNIVERSITÀ DI BOLOGNA

SCHOOL OF ENGINEERING

SECOND CYCLE DEGREE MASTER'S DEGREE IN AEROSPACE ENGINEERING

Class LM-20 – Aerospatial and astronautic engineering

EXPERIMENTAL ANALYSIS OF FATIGUE BEHAVIOUR AND METALLOGRAPHIC CHARACTERIZATION OF SC-AL COUPONS

Graduation Thesis in Aerospace Structures

Candidate

Federica Remor

Supervisor

Professor Enrico Troiani

Academic Year 2022/2023

To my family

Abstract

Materials and different technologies employed in the aerospace field play an important role. Aerospace materials can be described as structural materials that support the loads exerted on the aircraft throughout flight operations. Continuous research is carried out leading to an improvement in the quality of the materials used in this field. There is always the need for lighter materials that could be used in airframe structures. At the same time, these materials need to provide excellent strength. Aluminum alloys are widely used in airplane structures due to their variety of qualities that make them ideal for this application. Deep research has been done on aluminum alloys and continues up to this day. Fatigue analysis is part of this research and has been studied intensively to understand and gain better knowledge about fatigue behaviour and fatigue mechanism of these materials.

A full analysis of coupons made with Scalmalloy has been conducted in this study to evaluate the properties and functionality of this material. An in-depth literature review concerning the static and fatigue behaviour of Scalmalloy coupons has been done before proceeding with experimental tests. Static and fatigue tests were carried out and were then compared with the literature results. Metallographic analysis was then performed, including microscopic observations, fractography analysis, and additional procedures. This prepares the coupons examined for the study of their microstructures.

The objective of the thesis includes the complete fatigue and metallographic investigation of Scalmalloy coupons and their comparison with the literature review. This comparison allows the evaluation of the material properties and their reliability and from this analysis, other methods by which the work could be improved are suggested.

Index

List of Figures

List of Tables

1. Introduction

Designers are continuously looking for stronger and lighter materials to accomplish continuous performance developments. Light alloys are widely used in many industrial and engineering areas because light materials capable of supporting heavy loads are constantly in demand.

The most effective method for decreasing aircraft weight and enhancing performance has been demonstrated to be reducing material density. Lowering the density of a material is estimated to be three to five times more efficient than raising its tensile strength, modulus, or damage tolerance [1].

The first material considered for the construction of an airplane was wood. Subsequently, aluminum has been the most used material in airframes since the 1920s until composites were developed in the 1960s and 1970s when they were first used for military purposes. Commercial aircraft have followed similar tendencies, but more slowly and cautiously.

1.1 Light Alloys

Historically, magnesium and aluminum have been referred to as "light metals" due to their frequent application in reducing the weight of components and structures. Because of this, titanium is also acceptable, and even if beryllium is not used much, it should be included.

The relative densities of these four metals range from 1.7 g/cm^3 for magnesium to 4.5 g/cm^3 for titanium, compared to 7.9 g/cm^3 and 8.9 g/cm^3 for the two older structural metals, iron, and copper. Although several other elements that fall under the metals category are lighter than titanium, the majority of them are not used as a base material for structural applications.

A characteristic of lightness translates directly to improving material properties since a drop in density yields the largest weight reduction for several products. Light metals have naturally been linked to transportation, particularly aerospace, which has greatly aided in the development of light alloys during the past century.

Strength-to-weight ratios have also been a major consideration. The central positions of the light alloys based on aluminum, magnesium, and titanium in respect of other technical alloys and to all materials are illustrated in an Ashby diagram in Figure 1.

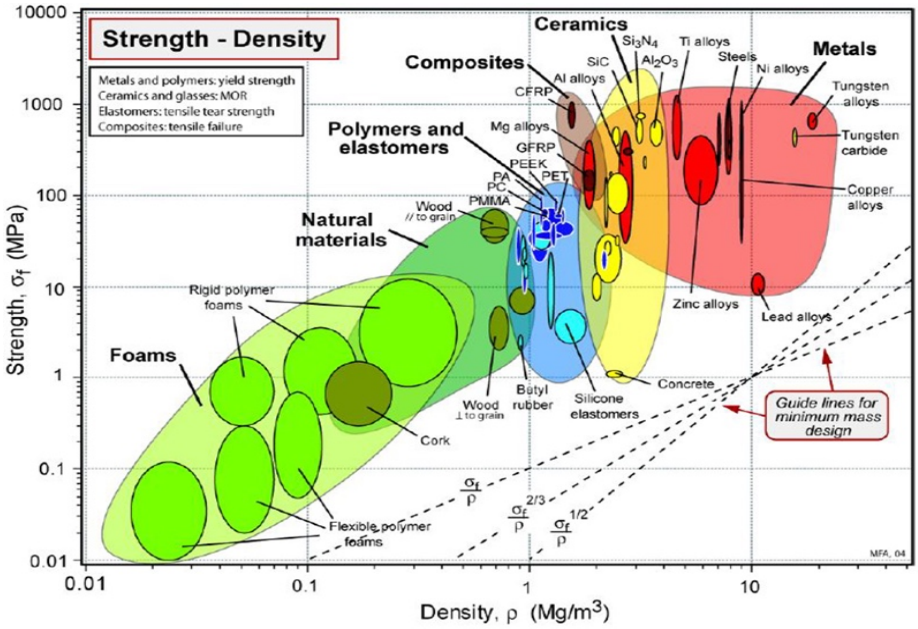

Figure 1 Ashby diagram [2]

Light metals have additional qualities that are highly significant for technology, and concerns about weight reduction should not overshadow this fact. Magnesium's castability and machinability, titanium's severe corrosion resistance, and aluminum's generally strong electrical and thermal conductivities are a few examples [3].

Since the early 1920s, when aluminum alloys began to replace wood, they have been the primary material used in airframe construction. High-strength aluminum alloys are and will continue to be, an essential airframe material, even though the function of aluminum in future commercial aircraft will probably be slightly limited by the increasing use of composite materials.

1.2 Beryllium

Beryllium is another incredibly light metal with a great variety of properties. However, beryllium must be processed using expensive powder metallurgy technology. Also, because beryllium dust and powder are toxic, beryllium costs are further increased by the need for controlled manufacturing environments and safety concerns when repairing or servicing deployed structures [1].

1.3 Magnesium

Aluminum alloys and magnesium alloys typically compete for structural uses. Magnesium alloys often have a lower modulus of elasticity and are not as strong as high-strength aluminum alloys. On the other hand, magnesium alloys are competitive in terms of specific strength and specific modulus since they are substantially lighter. They have a low density, good ductility, very good casting characteristics and poor fatigue resistance [4]. The main obstacle to the application of magnesium alloys is their incredibly low level of corrosion resistance [1].

1.4 Titanium

Heavy steel alloys in the airframe and superalloys in the low-temperature areas of gas turbines can frequently be replaced with titanium to reduce weight. In situations where aluminum cannot withstand temperatures beyond 150 °C or when corrosion or fatigue have been persistent issues, titanium is also used instead of aluminum.

Titanium's exceptional fatigue resistance, high-temperature capabilities, and corrosion resistance make it a more important component for airframes [1]. Also, they have intermediate density and show a good response to strengthening by age hardening and quench and temper heat treatments [4].

1.5 Aluminum

Aluminum is a lightweight, low-cost metal that can be strengthened to very high levels. It is also one of the more easily produced high-performance materials, which typically translates into reduced costs.

The primary characteristics of aluminum are:

- lightweight, with a density equal to 2,7 g/cm^3 which corresponds to a specific weight of approximately one-third of steel and copper;
- good fabricability;
- good ductility and malleability;
- high electrical and thermal conductivity;
- good corrosion resistance;
- low cost.

To enhance the mechanical properties, specific amounts of alloying elements are added to the aluminum. Some of the properties of aluminum alloys are:

- low specific weight, between 2,66 and 2,85 g/cm^3;
- low melting temperatures, between 510°C and 650°C;
- high electrical and thermal conductivity;
- cryogenic properties, at low temperatures, aluminum alloys do not embrittle and instead get stronger without suffering substantial ductility losses;
- high strength-to-weight ratio.

However, aluminum alloys come with some drawbacks, like low modulus of elasticity, low mechanical properties at elevated temperatures, and susceptibility to corrosion. Aluminum alloys typically have a modulus of elasticity of 70 GPa, which is less than that of comparable materials like

steel (215 GPa) and titanium (110 GPa). The long-term use temperatures of aluminum alloys are typically limited to 120°C to 150°C, but they can be used for short periods at temperatures as high as 205°C to 260°C. Lastly, corrosion can be an issue for the highly alloyed high-strength aluminum alloys used in aircraft, even though pure aluminum and many aluminum alloys are quite resistant to corrosion [1] [5] [6].

Aluminum alloys are first categorized into two groups depending on the component production processes: casting alloys and wrought alloys.

Casting alloys can be made specifically for a specific casting technique. The final metal structure is influenced by the casting techniques and alloy composition. Some might require heat treatments to improve their characteristics [6].

Wrought alloys are shaped by plastic deformation. Because they must meet distinct requirements during the manufacturing process, their compositions and microstructures differ greatly from those of casting alloys.

To separate alloys that are suitable for heat treatment from those that are not, another classification might be adopted.

Particularly for the aircraft sector, alloys incorporating *lithium* have been introduced. Significant improvements in mechanical properties can be obtained by adding lithium, although other characteristics may be compromised.

The alloy density decreases due to the low density of lithium, the modulus of elasticity is increased, fatigue resistance is enhanced, it has good toughness at cryogenic temperatures, strength equal to or greater than that of common alloys, and the ability to be superplastically shaped into complex shapes, It is also susceptible to cracking from stress corrosion [4].

1.6 Fatigue Study

When a material is subjected to conditions that cause fluctuating stresses and strains at one or more points, and which may result in cracks or complete fractures after a sufficient number of fluctuations, fatigue testing is defined [7]. This phenomenon is dangerous since the stresses that lead to fatigue failure are below the material's limits and would not harm the components if applied singularly.

A specimen subjected to a cyclic load may experience the initiation of a fatigue crack nucleus at a microscopic size, which can grow into a macroscopic crack before the specimen fails in the final cycle of its fatigue life.

An in-depth knowledge of the fatigue mechanism is necessary to consider many technical aspects, such as material surface quality, residual stress, and environmental effects, which affect fatigue life and fatigue crack propagation.

It is necessary to understand fatigue as a crack initiation process followed by a crack growth period to evaluate fatigue prediction systems.

Although some microcrack growth is expected to occur during the initial period, the fatigue cracks are still too small to be noticeable. The crack grows and fails in the second phase.

Since various practical conditions have a major impact on the crack initiation period but little or no impact on the crack growth period, it is technically significant to examine the crack initiation and growth periods independently.

1.6.1 Phases of the Fatigue Life

As can be seen from the phases shown in Figure 2, fatigue in metals is typically split into two phases: the initiation phase and the crack growth phase. The methods used to characterize or evaluate the two phases may vary based on the distinct mechanisms that influence the development and propagation of cracks in each phase.

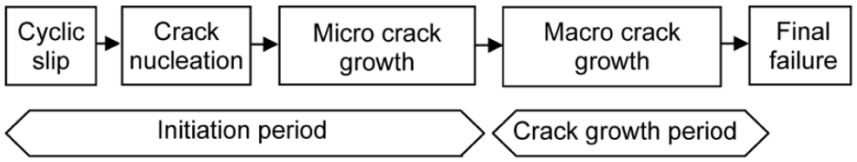

Figure 2 Phases of the fatigue life [8]

The creation or nucleation of microscopic cracks, which is primarily controlled by surface aspects, is covered under the initiation phase. The time at which such fatigue cracks occur is greatly influenced by surface quality or roughness as well as environmental factors like corrosion. Microcracks are invisible for a substantial amount of the fatigue life. The remaining fatigue life of a laboratory specimen is typically only a small portion of its total life once cracks appear.

For macroscopic cracks that propagate throughout the material, the time at which fatigue cracks occur is mostly controlled by how resistant the bulk material is to the cracks' growth [9].

It was discovered that microcrack nucleation often happens relatively early in the fatigue life. It has been found that if a cyclic stress higher than the fatigue limit is applied, this could occur nearly instantly. The cycle stress level below which a fatigue failure does not occur is known as the fatigue limit [8].

It should be noted that, while the majority of studies refer to the first phase as the initiation phase, several scientists have recently emphasized that it is more accurate to talk about fatigue crack nucleation, or more accurately, fatigue crack formation. It is argued that nucleation and formation allude to a more progressive action, which is what occurs in this phase, whereas initiation may refer to an instantaneous action.

1.6.2 Crack growth

For metallic materials, fatigue is associated with cyclic plastic micro-deformations brought on by the stress cycle. Locally, the stress value may exceed the yield strength due to discontinuities or defects in the material, which leads to fracture.

Crystals cohesive to one another constitute most metallic materials. Atomic planes are layered to form crystals. It is the irreversible slipping of these planes that causes the phenomenon of fatigue at the microscopic level. Usually, the component's surface is where the fracture happens.

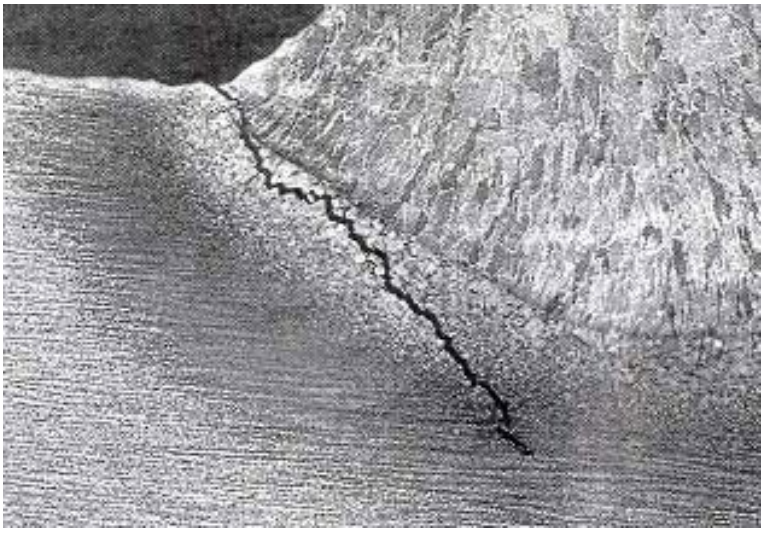

Figure 3 Fracture initiation [10]

The nucleation phase, which follows the initiation of the fracture, is when microintrusions and microextrusions give rise to fatigue damage. Microcracks are generated which tend to converge and form the actual crack. As it continues to ‘go through’ the component, the crack's size grows.

The nucleation phase results in the final fracture, when the progressive decrease in the resistant section caused by the crack's progression causes it to break with a crash since it can no longer withstand the applied loads.

An example of a sample’s fracture surface can be seen in Figure 4, in which two areas can be distinct: an area with growth bands and a smooth area of the final fracture.

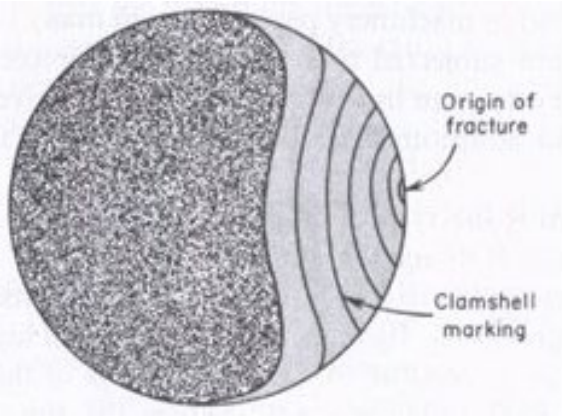

Figure 4 Fracture surface scheme [10]

1.6.3 Fractographic Analysis

The fracture surface of materials can be studied using fractography, a method used in failure analysis. The cause of an engineered product's failure can be discovered by examining the fractured surface's characteristics. Fractographic analysis of a fracture can provide important details that help understand the meaning of fatigue results from tests.

Establishing and examining the crack's origin is one of the primary objectives in fractography because it can reveal the reason behind the crack's initiation.

First fractographic analysis is often performed with an optical microscope on a macro scale. Optical microscopy or macro photography can frequently identify the type of failure and the causes that lead to the formation and propagation of cracks.

Inclusions, voids or empty holes in the material, contamination, and stress concentrations are common characteristics that may contribute to the start of a fracture.

The crack growth mechanism and initiation point can be identified with a microscope. SEMs, or scanning electron microscopes, are typically used for fractography examinations, which often require inspection at a finer scale. The optical microscope's resolution is significantly lower than this one.

Macroscopic and microscopic analysis frequently reveals concentric fracture surface markings surrounding the cracking origin. These markings are frequently helpful in determining the origin of the fatigue.

Groups of fatigue striations may be visible under a microscope, depending on the types of alloys. For instance, fatigue fracture surfaces of alloys such as nickel-base alloy, stainless steel, and aluminum frequently exhibit striations [11].

2. Additive Manufacturing

The official industry standard title (ASTM F2792) for all the technology applications that will be presented is additive manufacturing. Rather than using subtractive manufacturing techniques, it is defined as the process of joining materials to create objects from 3D model data, usually layer by layer [1]. The ability to build almost any shape that would be extremely challenging to machine, human involvement, and the reduction of time and cost are some of the significant improvements this approach brought to product development [12].

The basic goal of additive manufacturing (AM) is to build a three-dimensional object from a model created by computer-aided design (CAD). This presents an unprecedented chance to digitize the manufacturing sector. The potential for obtaining improved flexibilities with this technology has significantly grown thanks to a variety of software and technological platforms, greater computational power, and connectivity.

In addition, it contributes to the advancement of design accuracy and reliability as well as the development of customized manufacturing for products with almost limitless design flexibility. Also, it has expanded into large-scale production and large-part printing [13].

The use of fibre reinforcement in 3D-printed plastics and resins to enhance their mechanical properties has contributed to AM's growth in the production of polymer composites.

2.1 Process of Additive Manufacturing

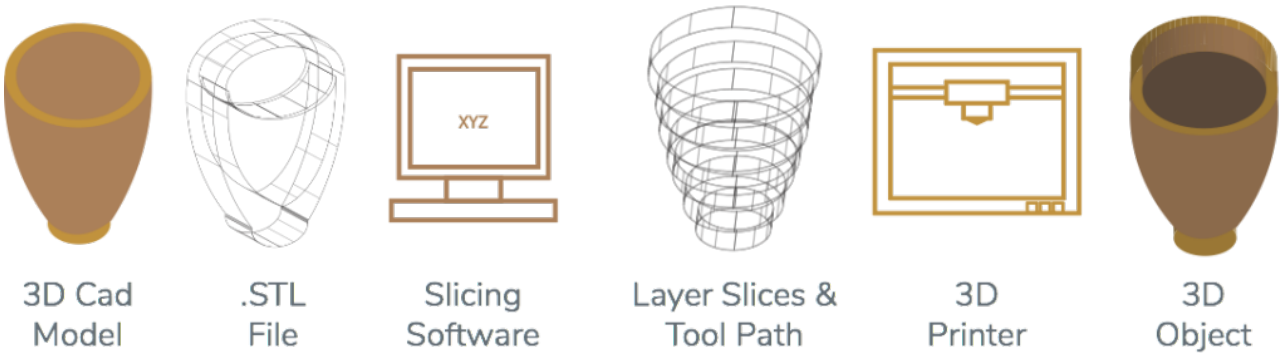

Figure 5 Steps of the additive manufacturing process [14]

The additive manufacturing technique is composed of several steps that lead the project from CAD to the component's full realization. Firstly, a CAD model needs to be developed and from this, a mesh is created. This means incorporating design guidelines to adjust the initial digital model to the machine requirements like scale factors or minimum thickness. The mesh is saved as an STL file which uses a shell-type model to approximate the object's outside surface. Triangles of varying sizes are used to recreate the geometry [15].

After this, a set-up for processing parameters is chosen including the building direction, slicing and the creation of supports. The main roles of the supports are to support protruding sections, protect the side walls of the component from actions that might compromise its construction, anchor the model under development to the work area while still permitting its later removal and remove the component's distortion effect caused by residual stresses.

The component is then sliced, ideally into sections that run parallel to the construction plane.

Production can begin and the machine can be left to operate without human supervision because it is essentially an automated process. Manufacturers of AM printers are currently implementing and integrating process control software, through automated surveillance systems, which can monitor production progress and immediately stop it if defects are discovered that would seriously impair the final component's quality.

The produced object needs to be taken out of the machine so that finishing and post-processing can take place. This phase will involve removing the supports, which can be done mechanically for most metal components or, for some polymer-produced components, by dissolving them in water solutions. and a post-treatment is needed once the desired object has been built [15].

2.2 Additive Manufacturing Techniques

The range of additive manufacturing techniques can be divided into several categories using a set of standards developed by ASTM (ISO/ASTM 52900:2015). Some of these AM procedures are jetting, binder jetting, vat photopolymerization, powder bed fusion, material extrusion, energy deposition, and sheet lamination.

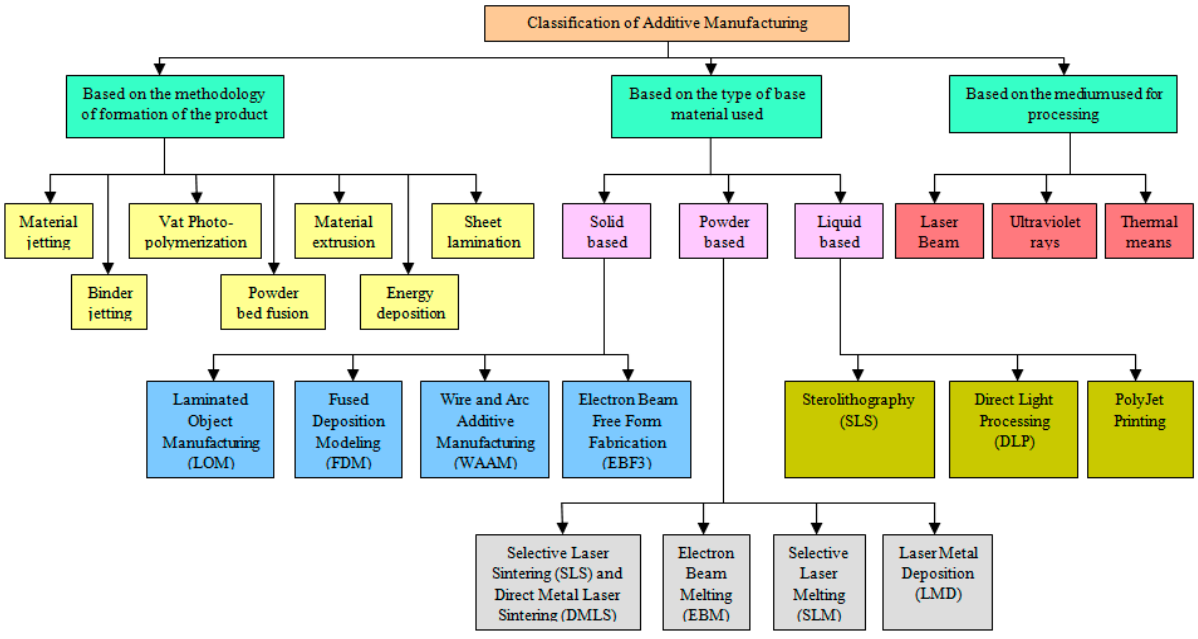

Figure 6 Classification of Additive Manufacturing Techniques [13]

Based on the physical state of the material used and processed to create the product, AM may be further categorized. Processes based on solid, liquid, and powder are included in this classification, as can be seen in Figure 6. It is further classified according to the medium used in processing the base material, such as heat, laser beams, and UV rays.

Numerous factors, including built volume, cost, quality, surface finish, resolution, fabrication speed, and part strength, are taken into account while evaluating AM methods. They are always changing to create larger, more complex products in a more economical and flexible approach. However, the production speed and resolution are the two most important factors. Consequently, these two process parameters are frequently used to evaluate AM processes [13].

The structure is constructed "layer-by-layer" into the desired shape. A vast variety of materials, including combinations in the form of composites and metallic, ceramic, and polymer materials, can be used to adapt the process to most industrial sectors.

Some techniques are presented in the next subparagraphs.

2.2.1 Stereolithography

The first AM technique to be developed was stereolithography (SLA). Using a UV laser, a photosensitive polymer resin is exposed to create the part. The layer is formed when the photosensitive resin solidifies in the presence of an ultraviolet laser. After this, layers are created by lowering the build platform and exposing the resin following the CAD data [13].

A CAD model is used for the first step in the process, after which it is converted into an STL file, and the components are "cut in slices" revealing the information of each layer [12].

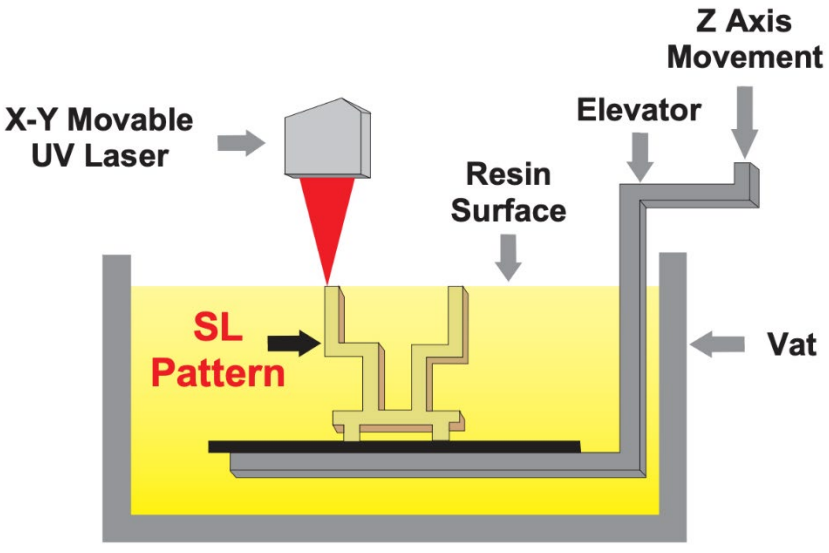

Figure 7 Stereolithography scheme [16]

2.2.2 Powder Bed Fusion

Powder bed fusion (PBF) is an additive manufacturing in which by using a high-energy source, metallic powder is melted to create objects layer by layer. Particle powder is selectively scanned and fused at predefined areas on a powder bed using a heat source (laser or electron beam) that can be controlled with power, speed, and scanning strategy.

The PBF process has multiple variants, each identified by the type of material and heat source used. Selective laser melting (SLM), selective laser sintering (SLS), and electron beam melting (EBM) are the three main categories of this method. There are benefits and drawbacks to each variation, hence suitability is determined by the specific use.

Selective laser sintering is also known as laser beam powder bed fusion (LB-PBF). By creating consecutive layers of powder materials on top of one other, powdered polymer materials are sintered using a laser beam to form layers. Preheating is the first step in the LPBF process, and it ensures that the platform temperature stays below the glass transition temperature of the materials. Preheating has several advantages, including decreasing internal residual stresses on built samples, increasing the capacity to manufacture a variety of powders and fabricate complex shapes without sacrificing dimensional accuracy, and reducing the requirement for laser energy.

To prevent oxidation and contamination, the LPBF operates in a building chamber with inert gas protection.

The LPBF technique is notable for its rapid heating and cooling rate because the laser interacts with a small volume of powder for only a short amount of time. The nucleation rate is facilitated, grain development is suppressed, and the metastable phases are formed when heating and cooling rates are high.

The melt pool mode, heating temperature gradient, and cooling (solidification) rate during the LPBF process can be significantly influenced by many factors. These factors include laser power and scanning speed, layer thickness, hatching space, scanning strategies, powder size, wettability, morphology, and melt pool dynamics and stability. The energy provided by the laser during a single-layer scan in LPBF is often estimated as the power absorbed by a specific volume of bulk powder [17].

Layers are built one after the other until the last part is finished. Every time a layer is completed, the piston that controls the bed, which contains the particles, is lowered by the same amount as the layer thickness. A levelling roller pushes material across the build platform [13].

A wide range of materials, including plastics, metals, metal combinations, metal and polymer combinations, and metal and ceramic combinations, can be employed in this procedure. The broad range of materials that can be used and the ability to recycle wasted powder are the key benefits of this technique [12].

The model is finished by smoothing the exposed surfaces and removing any loose material once it has been taken out of the chamber. The powder that surrounds the pieces during processing accomplishes component support and it might be reused for other printing processes.

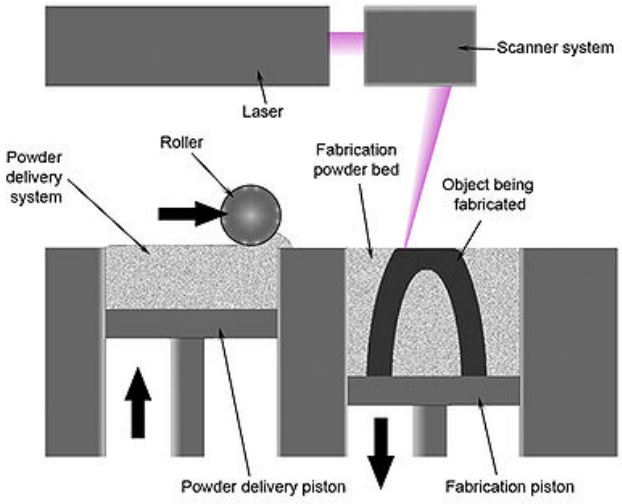

Figure 8 Selective Laser Sintering scheme [18]

A major factor in defining the final microstructure of the product created with LPBF is the extremely complex and dynamic heat distribution inside the melt pool. In the study 'Understanding melt pool characteristics in laser powder bed fusion: An overview of single- and multi-track melt pools for process optimization' the schematic diagram of the temperature variation of the platform and the pore creation are presented [17].

The area of superheated molten metal close to the laser/material interface is known as the melt pool (or molten pool); it usually takes the shape of a spherically shaped droplet that travels at the traversal speed. A melt pool is a thermodynamically unstable area, changing shape and internal energy as a result of interactions between liquids and solids and surrounding heat transmission. It is blown into the metallic powder while the laser uses energy transfer to make sure it survives. Since the melt pool is where the solid part begins, quality control is very interested in its morphology and temperature [19].

Direct measurement of the temperature in the melting zone is difficult due to the fast heating and cooling behaviour. A sensor was used to measure the substrate's temperature beneath the building

platform. After that, temperature data from the platform were plotted to obtain temperature curves for the substrate zone.

The temperature variations of the building platform during LPBF and EBM processes are depicted in Figure 9, and they have a significant effect on the molten fluid's thermal gradient and rate of cooling.

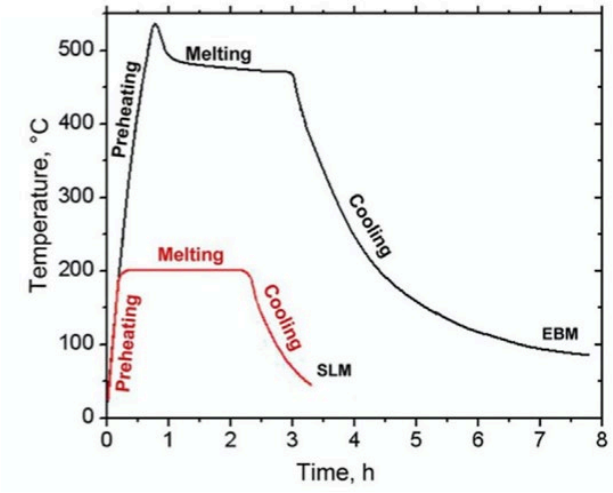

Figure 9 Temperature variation of the platform [17]

As a result, the melt pool's surface tension increases quickly while the temperature falls. Pore defects originate from the trapped metal vapor bubbles when the recoil pressure (metal vapor pressure) is lower than surface tension. This is shown in Figure 10.

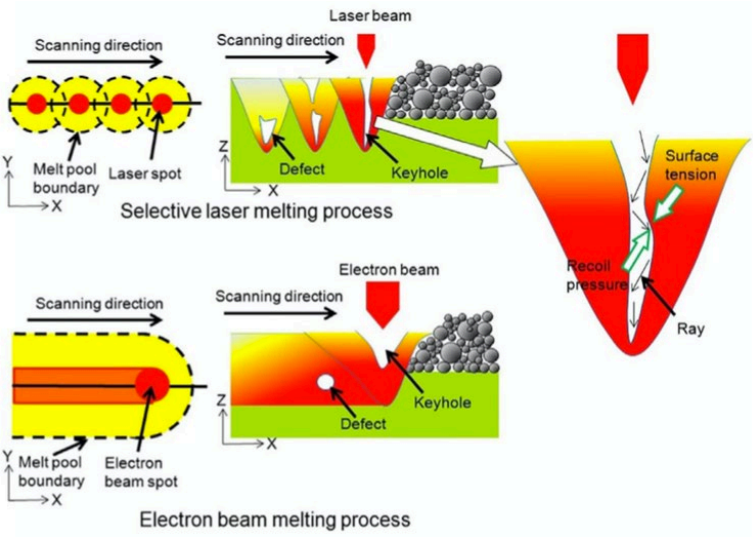

Figure 10 Pore creation schematic diagram [17]

The final quality of components produced by LPBF is influenced by the solidification of molten powder and the consolidation of layers, both of which are greatly influenced by the melt pool status.

Also, it is essential to properly examine the scanning speed, laser power, powder layer thickness, and hatching space, all of which have a significant impact on the end product's quality.

Electron beam melting (EBM) is similar to selective laser sintering, but an electron laser beam with a high voltage is used in this procedure to melt the powder [12]. The procedure is carried out in a chamber with a high vacuum.

2.2.3 Binder Jetting

Binder jetting (BJ) is an additive manufacturing technique where a liquid bonding agent is released onto the build platform to connect the layers of powdered particles that have been put there. An inkjet print head is created to drop the bonding liquid onto the powdered particles that are positioned on the platform. The platform goes downward to form the subsequent layer after the first layer has formed [13].

Because of its similarity to the inkjet printing method used for two-dimensional printing on paper, this procedure is known as 3D Printing (3DP) [12].

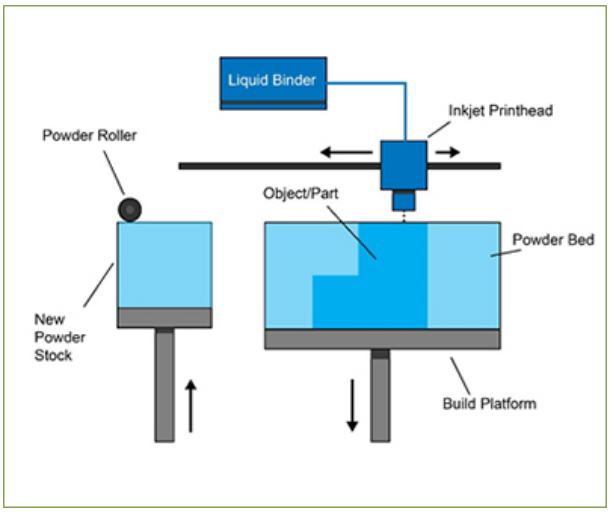

Figure 11 Binder Jetting scheme [20]

2.2.4 Fused Deposition Modeling

In the additive manufacturing method known as fused deposition modeling (FDM), a thin plastic filament is fed into a machine where a print head melts and extrudes through a nozzle. After melting, the material is placed on the build platform and allowed to cool and solidify. Layer upon layer, the part is constructed.

The primary benefits of this procedure are no chemical post-processing, that it doesn't require resins to cure, and uses less expensive equipment and materials, making it a more economical method. The drawbacks include a low z-axis resolution in comparison to other additive manufacturing processes, necessitating a finishing process if a smooth surface is needed, and a lengthy process that can take days to complete big, complex objects [12].

To support overhanging structures and secure the components on the build platform, support structures are needed and these can be built with a different material. [1]

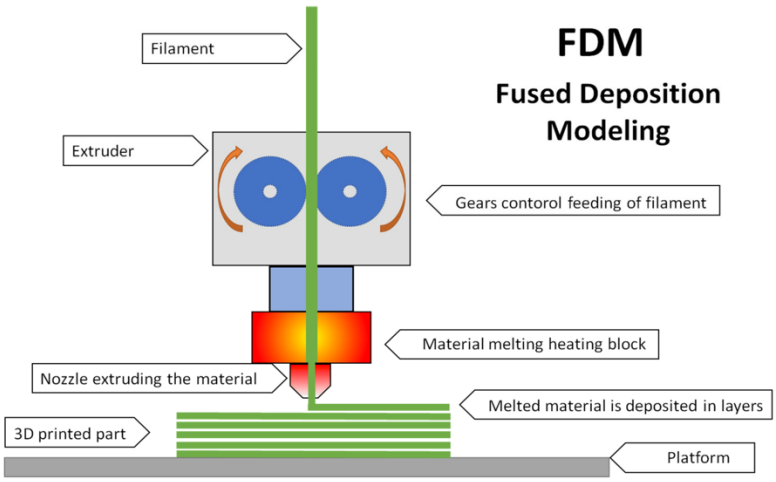

Figure 12 Fused deposition modeling [21]

2.3 Scalmalloy in Additive Manufacturing

Over the last decade, research on powder bed fusion processing of Al alloy powders has grown significantly, making them one of the most studied metal alloys for LB-PBF.

Recently, Al-Sc alloys have been studied, primarily at a low technology readiness level (TRL) level, for the production of PBF materials. However, the TRL of this research is typically poor. The Airbus Corporate Research Center (Airbus Group Innovations) claims that Al-Mg-Sc alloy (Scalmalloy) is the first metal powder designed especially for additive manufacturing.

Originally developed by Airbus APWorks and a few collaborators, this Al-Mg-Sc alloy is now widely available for use in the automotive and aerospace industries worldwide.

High cooling rates and rapid solidification lead to the creation of a peculiar microstructure that performs on the same level as the best aluminum foundry products. It is possible to create high-performance parts with an excellent level of functionality by combining these material qualities with the design freedom offered by AM methods.

Compared to AlSi10Mg, the Al-Mg-Sc alloy exhibits better static properties and the elongation at break is about twice larger. Strong processability and corrosion resistance are also noted.

By changing the minimum weight percentages of Mg and Sc from 4 to 4.5% and 0.6 to 0.68%, respectively, this specific Al-Mg-Sc powder evolved. This is to ensure that there is magnesium, which significantly decreases during the laser fusion process, as well as Scandium, which is required to improve the alloy's properties. In particular, it provides hardening effects through the formation of a

large family of Al-Sc-Zr/Al-Mg-Si-Sc-Zr and Al-Mg-Si-Cu-Sc-Zr precipitates along with the Zr contain.

On the contrary, the maximum values allowed for Si and Fe were lowered from 0.4% to 0.2% in each instance. This has been done to prevent the formation of eutectic Si particles or coarse and brittle Al-Fe-Mg phases. Particular attention should be given to the quantities of oxygen (O) and hydrogen (H) since too much of either element might compromise the alloy's mechanical qualities and primarily reduce its elongation [22].

Therefore, during manufacture, an argon environment that is stable and pure is necessary.

2.3.1 Properties of Scalmalloy

Scalmalloy is lightweight, it has high strength with good ductility, good corrosion resistance and high thermal conductivity. Its composition is shown in Table 1 [23]:

Aluminum	Balance	**Magnesium**	4.20 to 5.10 %	**Scandium**	0.60 to 0.88 %
Manganese	0.30 to 0.80 %	**Zirconium**	0.20 to 0.50 %	**Iron**	0.40 %
Silicon	0.40 %	**Zinc**	0.25 %	**Titanium**	0.15 %
Copper	0.10 %	**Vanadium**	0.10 %	**Oxygen**	0.05 %

Table 1 Chemical composition of Scalmalloy

Its application finds use in a variety of industries, such as marine, aerospace, automotive, and defence.

It has tensile strength equal to 520 MPa, yield strength of 480 MPa and an elongation of 13%. Its density is 2,67 g/cm^3 and the elastic modulus is 70 GPa. It has excellent corrosion resistance and high strength with good conductivity and high ductility. The powder has nominal particle size in the range between 20 and 63 μm.

The addition of Scandium in the alloy enables the process of precipitation hardening in the alloy and this affects the properties of the Scalmalloy. Al_3Sc developed as extremely fine particles, which will result in a very uniform precipitate distribution in the solution. This increases the alloy's strength, by 40-50 MPa per 0.1 wt.% Sc.

The Al_3Sc particles are beneficial for the weldability of the alloy, are useful for grain refinement and for the weldability of the alloy [24].

Scalmalloy exhibits a remarkable bimodal microstructure made by a fine-grained (FG) area and a coarse-grained (CG) area and the field of materials science is becoming quite interested in this specific microstructure [25].

3. Static Analysis

The studies 'A comparative investigation on the microstructure and mechanical properties of additively manufactured aluminum alloys' [26] and 'Structural integrity of additively manufactured aluminum alloys: Effect of build orientation on microstructure, porosity and fatigue behaviour' [27] are considered as they report the results of static tests done on Scalmalloy.

Afterwards, a static analysis test has been done on Scalmalloy coupons and the results are included in [28].

3.1 Static Analysis Literature

3.1.1 Chemical Composition, build layout, heat treatment and roughness

All the specimens have the chemical composition shown in Table 2 and they were built using the Laser Beam - Powder Bed Fusion technique with specific process parameters shown in Table 3:

Alloy Element	Scalmalloy
Al	Bal.
Si	0.20
Fe	0.10
Cu	–
Mn	0.50
Mg	4.60
Ni	–
Zn	–
Pb	–
Sn	–
Ti	–
O	0.04
Sc	0.70
Zr	0.30
Be	–
Minimum Particle Size	20 μm
Maximum Particle Size	63 μm
Powder Manufacturer	Carpenter Additive®

Table 2 Scalmalloy Chemical Composition

Alloy	Laser power (W)	Laser scan speed (mm/s)	Hatching distance (mm)	Layer thickness (mm)
Scalmalloy	370	1000	0.10	0.03

Table 3 LB-PBF process parameters

The Scalmalloy powders were provided by LPW technology (now Carpenter Additive) and no surface process parameter optimization was done for the Scalmalloy.

The Scalmalloy specimens of the first study [26] were cylindrical rods with 12 mm and 10 mm diameters, with 90 mm height and they were further machined with the shape shown in Figure 13.

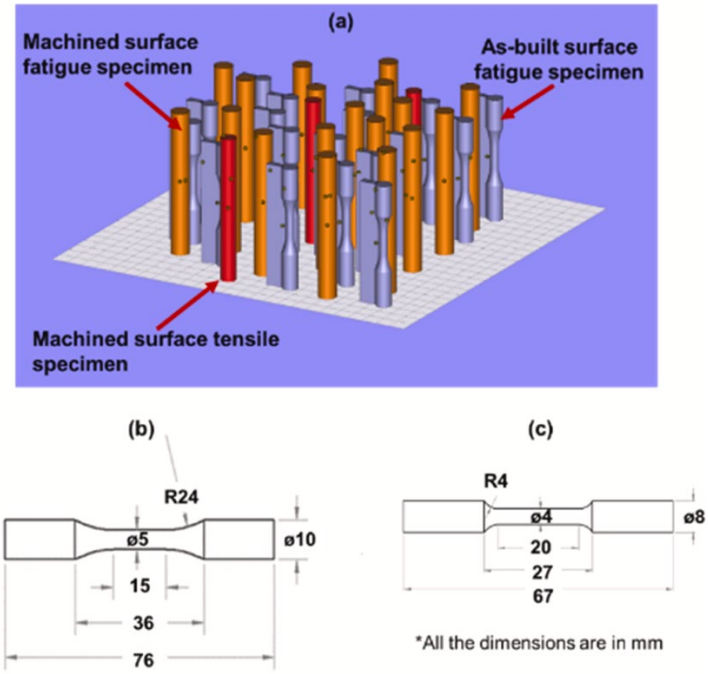

Figure 13 Print layout and final geometry of the specimens [26]

In the second study, specimens constructed as 90 mm long and 12 mm diameter cylindrical rods were fabricated in both vertical (V) and horizontal (H) orientations [27]. Whereas the horizontal specimens were constructed on top of support structures, the vertical specimens were deposited directly onto the build plate. The build layout is shown in Figure 14 as well as the final geometry reached after heat treatment and machining.

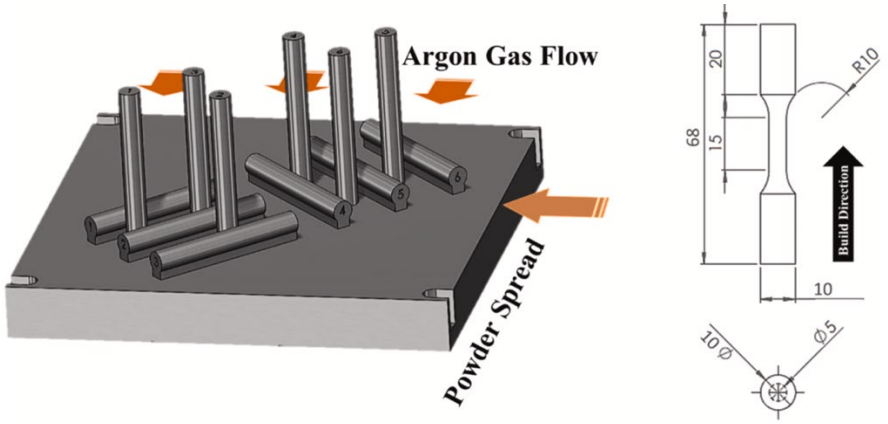

Figure 14 Build layout and final geometry of the specimens [27]

The specimens of both studies were heat-treated after fabrication using the procedure listed in Table 3.

Alloy	Temperature (°C)	Duration (hour)	Quenching environment
Scalmalloy	325	4	

Table 4 Heat treatment procedures of the first study

Alloy	**Temperature (°C)**	**Duration (hour)**	**Quenching Environment**
Scalmalloy	325	4	Furnace

Table 5 Heat treatment procedures of the second study

The heat treatments were applied after fabrication, before being cut from the build platform to avoid distortions during cutting due to the residual stresses, which are removed with the heat treatments.

The formation of $Al_3(Sc, Zr)$ precipitates has been reported after the thermal treatment and a maximum hardness has been noted [26].

Scalmalloy has a high roughness as can be seen in Figure 15. This results from the first study, because non-optimized surface process parameters were used during the fabrication of the Scalmalloy specimens, so their surface roughness is significantly higher.

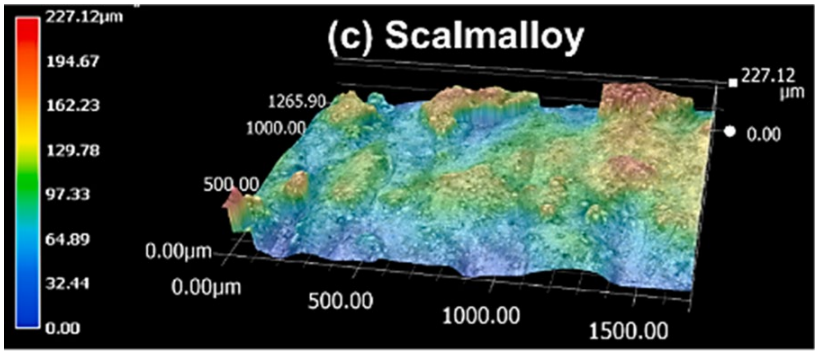

Figure 15 Representative surface roughness profile of Scalmalloy in the as-built surface condition [26]

3.1.2 Mechanical testing

The specimens were subjected to tensile testing using an MTS landmark servo-hydraulic load frame with a 100 kN load cell. The strain was measured using an extensometer attached to the specimens in the gauge section. Uniaxial fully-reversed ($R = \frac{\varepsilon_{min}}{\varepsilon_{max}} = -1$) strain-controlled fatigue tests were performed in both studies following the ASTM E606 testing standard.

Fatigue tests were performed at strain amplitude levels between 0.00075 and 0.0030 mm/mm for the as-built surface specimens and between 0.0010 and 0.0050 mm/mm for the machined surface specimens of the first study. These tests were carried out on specimens until they completely broke into two pieces (final fracture). Tests for runout stopped for specimens that had more than 10^7 reversals.

In the second study, fatigue tests were conducted for two different strain amplitude levels of 0.002 mm/mm and 0.003 mm/mm. The extensometer was fastened to the gauge section to regulate the tests and measure the strain there.

The curves presented in Figure 16 report the results of the engineering strain and the displacements investigated in the first study are in Figure 17. Other materials are investigated in this study and their curves are visible in these plots.

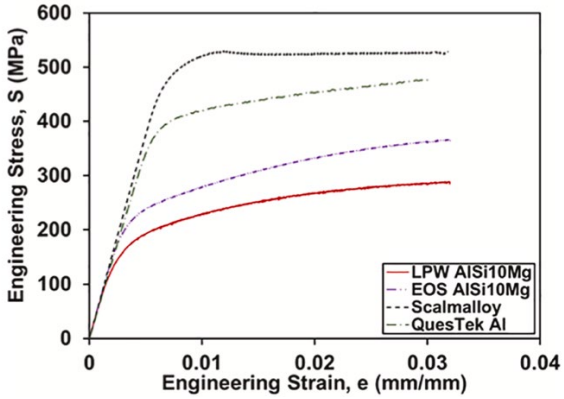

Figure 16 Engineering strain results of the first study [26]

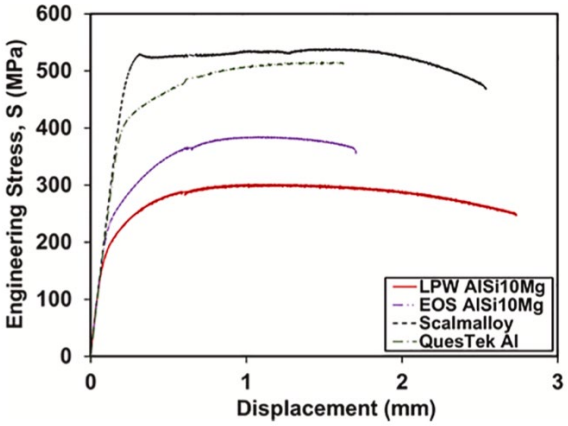

Figure 17 Displacement results of the first study [26]

All the results are listed in Table 6, where Sy, is the yield strength, Su is the ultimate tensile strength, E is the modulus of elasticity, $\%El$ is the percent elongation, ε_f is the true fracture strain or ductility and $\%RA$ is the percent reduction in area.

Alloy	Heat treatment	S_y (MPa)	S_u (MPa)	E (GPa)	$\%$ El	ε_f	$\%$ RA
LB-PBF Scalmalloy	325 °C, 4 h	508	530	77	16	0.44	35

Table 6 Tensile testing results of the first study

The Scalmalloy has a high tensile strength (given by Sy and Su) and a high ductility which can be explained by the material's precipitation hardening behaviour and ultrafine/nano-size grain structure.

3.1.3 Presence of nano-size grains and precipitates

Scalmalloy's high strength and high ductility are justified by its microstructure, grain size, and the presence of precipitates. The yield strength, Sy, is inversely related to the grain size, meaning that Sy increases as grain size decreases, according to the Hall-Petch relationship. Consequently, the presence of ultrafine/nano-size grains in the LB-PBF Scalmalloy's microstructure, produced during the building process and the post-heat treatment, is one explanation for its high Sy. Also, the formation of precipitates can enhance the strength of the Al alloy [26].

Figure 18 illustrates the fine grains of the LB-PBF Scalmalloy and the nearly uniform dispersion of nano-size $Al_3(Sc, Zr)$ precipitates which are indicated by red arrows.

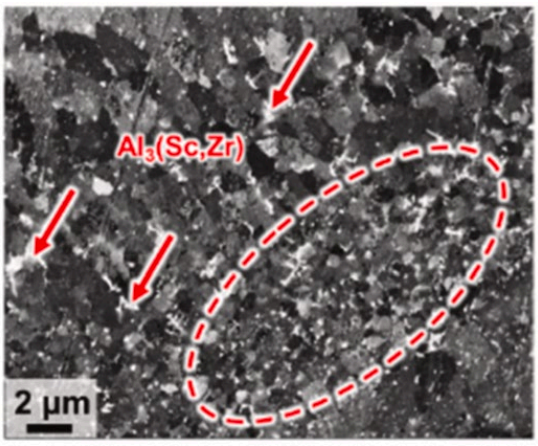

Figure 18 ECCI micrographs of the Scalmalloy

3.1.4 Surface irregularities

It is commonly known that surface roughness contributes to stress concentration on the surface, which may lead to earlier fracture initiations. Numerous studies have demonstrated that the rough surface of as-fabricated AM parts can cause multiple fracture initiations from micro-notches, which reduces the fatigue performance of the specimens. Scalmalloy specimens perform excellently in terms of fatigue while having a high level of surface roughness as well. This is because Scalmalloy's microstructure contains coherent nano-size precipitates in addition to an ultrafine/nano-size grain structure.

Figure 19 shows the tensile fracture surface of the first study. It shows the fibrous fracture surface of Scalmalloy, which exhibits deep and broad dimples in addition to fine ones, signifying the material's ductile rupture.

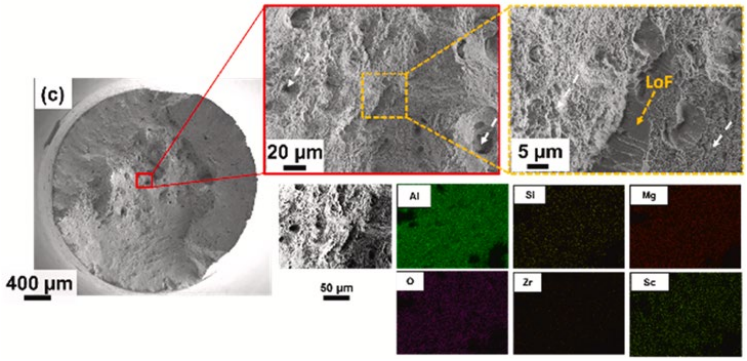

Figure 19 Tensile fracture surface of the Scalmalloy of the first study [26]

Usually, pores and LoF are the cause of the crack initiation in AM materials. But also, the cracks can initiate from the surface. The volumetric defects' shape, size, and location, with regard to the

specimen's surface boundary, also affect the fatigue life in the end. The fatigue life is usually shorter the larger and closer the defects are to the surface.

Figure 20 and Figure 21 display a chosen fracture surface for Scalmalloy tested at 0.0020 mm/mm strain amplitude to comprehend the failure mechanisms of the alloy in the as-built surface condition.

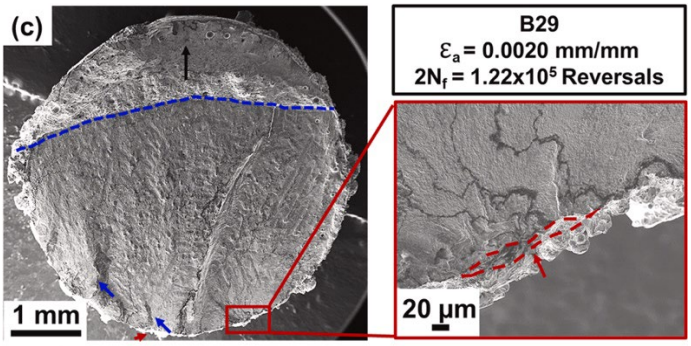

Figure 20 Fracture surface of the Scalmalloy in the first study [26]

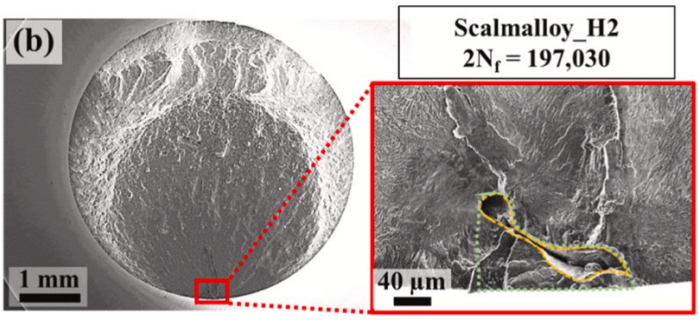

Figure 21 Fracture surface of the Scalmalloy of the second study [27]

The average $\sqrt{area}$ of the Scalmalloy specimens' defects in the first study is 64 µm while in the second study is almost 54 µm. The LoF defect shown in Figure 21 has a $\sqrt{area}$ equal to 102 µm. Most of the defects were in the range of 20-30 µm, but fatigue cracks usually initiate from larger ones.

3.1.5 Porosity

Figure 22 shows the X-ray CT scan results in the gauge section of a vertical and horizontal Scalmalloy specimen of the second study. The horizontal specimen has more volumetric defects than the vertical one and this could be explained by the different thermal history that the horizontal and vertical specimens encountered. But in this case, the difference is not so high, and the thermal properties of the alloy may be responsible for this, like low thermal diffusivity and conductivity. Also, large porosity can derive from the process settings employed to create Scalmalloy which were not optimized [27].

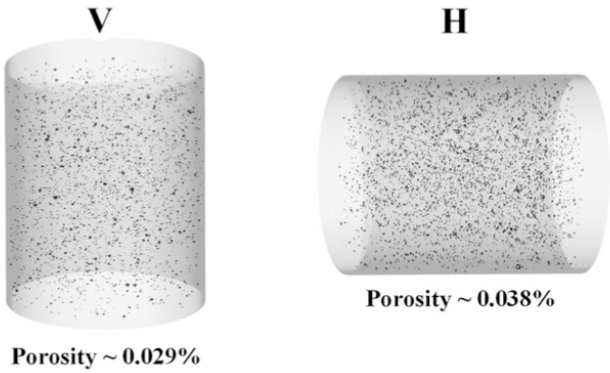

Figure 22 Porosity in vertical and horizontal specimens

3.1.6 Microstructure

The microstructures of the heat-treated Scalmalloy specimen of both studies are shown in Figure 23 and Figure 24 presented below.

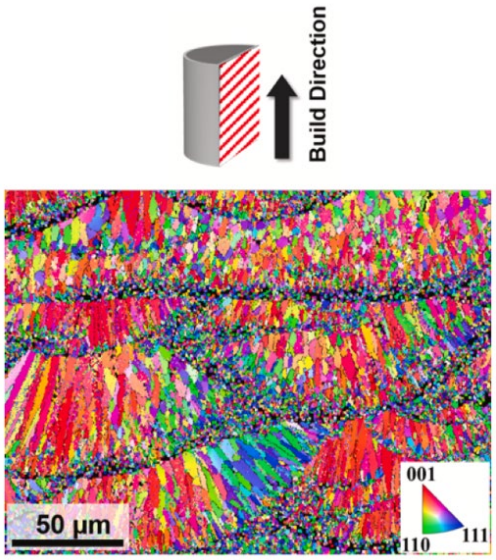

Figure 23 Microstructure characterization on the longitudinal plane parallel to the build direction of the Scalmalloy specimen of the first study [26]

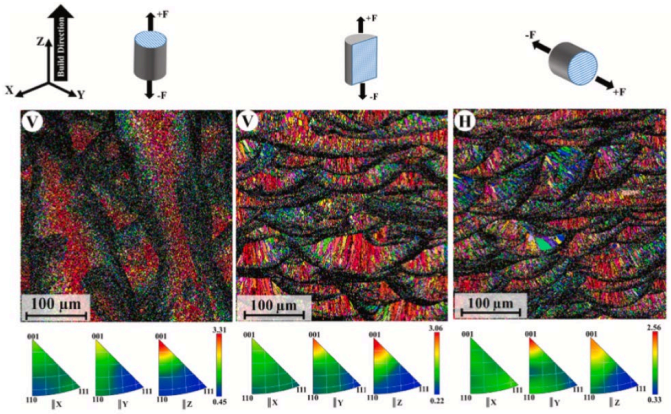

Figure 24 Microstructure of vertical and horizontal Scalmalloy specimen of the second study [27]

It is evident that Scalmalloy has an extremely fine grain structure made up of ultrafine/nano-size equiaxed grains as well as more refined columnar grains. The mean grain size for Scalmalloy

measured in the first study is 2.3 µm. The development of coherent nano-size $Al_3(Sc)$ and $Al_3(Zr)$ precipitates during the fabrication process is responsible for the material's highly refined microstructure. These precipitates act as heterogeneous nucleation sites and prohibit grain growth by pinning the grain boundaries, which results in grain refinement [26].

3.1.7 Observations

It was found that the volumetric defects, like pores and LoF, and the microstructure, which includes grain size and precipitates, could significantly affect the tensile and fatigue behaviour of the Scalmalloy.

Fine columnar grains and nano-size equiaxed grains made up the Scalmalloy. The formation of coherent nano-size $Al_3(Sc, Zr)$ precipitates during fabrication was attributed to the grain refinement in the Scalmalloy.

Scalmalloy exhibits high tensile strength and high ductility. This behaviour was related to the development of additional nano-size precipitates following heat treatment, as well as the existence of ultrafine/nano-size grain structure and nano-size precipitates from the manufacturing process.

Scalmalloy presents also a high fatigue resistance in both as-built and machined surface conditions.

Fatigue crack initiations were discovered to be caused by surface micro-notches in the as-built surface specimens. On the other hand, with the machined surface state, the volumetric defects, pores or LoF, were the source of the cracks.

3.2 Static Testing

3.2.1 Chemical Composition, Printing Layout and Samples Geometry

The table below shows the precise chemical composition of the powder that was used [23].

Aluminum	Balance
Manganese	0.30 to 0.80 %
Silicon	0.40 %
Copper	0.10 %
Magnesium	4.20 to 5.10 %
Zirconium	0.20 to 0.50 %
Zinc	0.25 %
Vanadium	0.10 %
Scandium	0.60 to 0.88 %
Iron	0.40 %
Titanium	0.15 %
Oxygen	0.05 %

Table 7 Scalmalloy Datasheet

The laser power and speed used for the printing layout are 175 W, 800 mm/s, 70 µm for the hatch space, and 20 µm for the thickness layer. For printing, the laser uses a checkerboard pattern with 3x3 mm^2 squares. The scanning strategy is required to keep the temperature as constant as possible. The aim is to prevent excessive stresses from deforming the specimens.

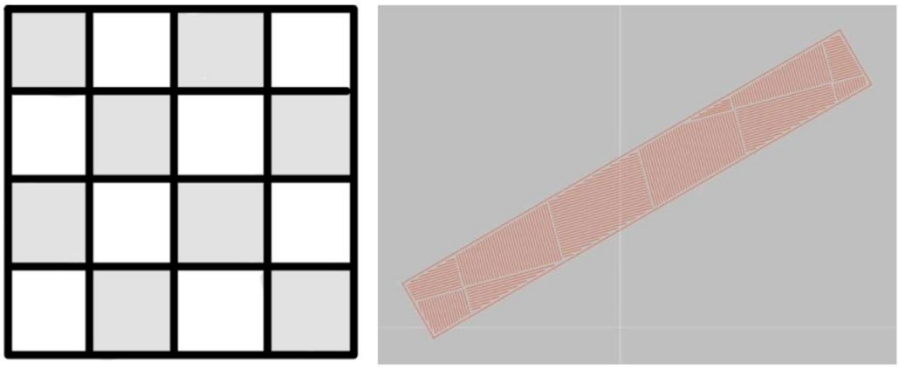

Figure 25 Scanning strategy

The laser alternates its orientation between adjacent squares and prints the squares in a random order. Furthermore, the laser modifies the zero by executing a roto-translation in between the scanning of two neighbouring layers.

During the sample production process, supports that connect the specimen to the printing bed must be employed. In addition to providing support, they exchange heat with the base to avoid the creation of excessive temperature gradients. The supports are created together with the specimens but with different parameters: laser power 150 W and laser speed 1100 mm/s.

Printing orientation influences production costs and sample production times. Printing in a vertical configuration takes longer than printing horizontally, but more specimens can be produced.

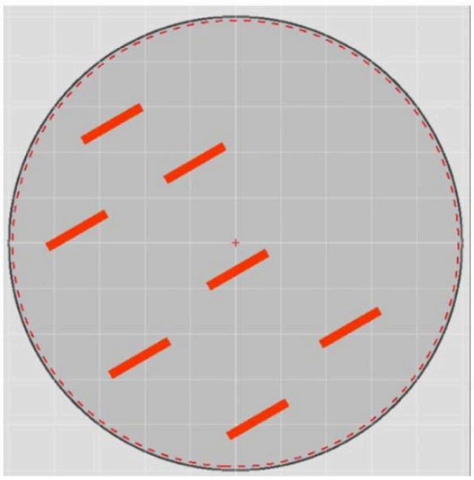

Figure 26 Printing orientation

Three of the six samples were printed as-built (AB) and three were heat-treated (HT) utilizing the chosen horizontal print orientation with the L-PBF.

The samples were heated to 325°C for four hours, and then they were gradually cooled in the oven.

The table and pictures below show the samples' geometry [28].

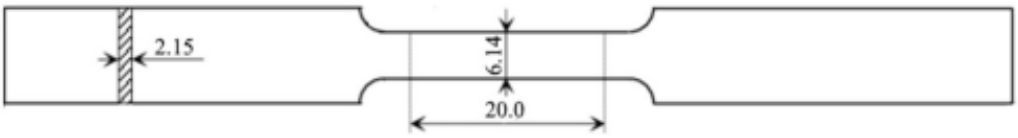

Figure 27 Geometry of the samples

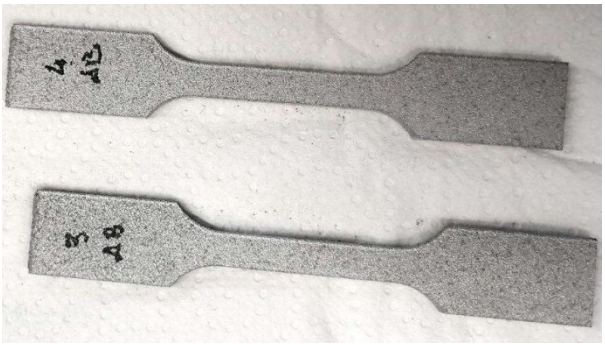

Figure 28 Scalmalloy samples

3.2.2 Mechanical Tests

Different tests were performed: tensile testing, an optical microscope microstructure analysis, and Vickers microhardness tests.

3.2.3 Tensile Testing

An extensometer was used to measure the test's deformation during the tensile testing, which was carried out using an ITALSIGMA servo-hydraulic machine with a load cell of 100 kN. Three AB samples and three HT samples underwent tensile testing.

The percentage elongation was obtained using the extensometer, and the fracture strength was calculated using the load cell data. The equations (1) and (2) were used in their calculations:

$$Stress\ [MPa] = \frac{load\ [kN] * 1000}{area\ under\ resistance\ (b * h)} \tag{1}$$

$$\%\ Elongation = strain\ \left[\frac{mm}{mm}\right] * 100\% + k \qquad where\ k = cost \tag{2}$$

Table 8 contains a list of the collected data [28].

	AB 1	AB 2	AB 3	HT 1	HT 2	HT 3
UTS [MPa]	329.22	324.29	329.22	448.45	464.81	462.39
YS [MPa]	248	250	280.5	426	430	435
% Elongation	13.41	13.14	12.68	1.83	6.80	3.09

Table 8 Tensile Testing Data

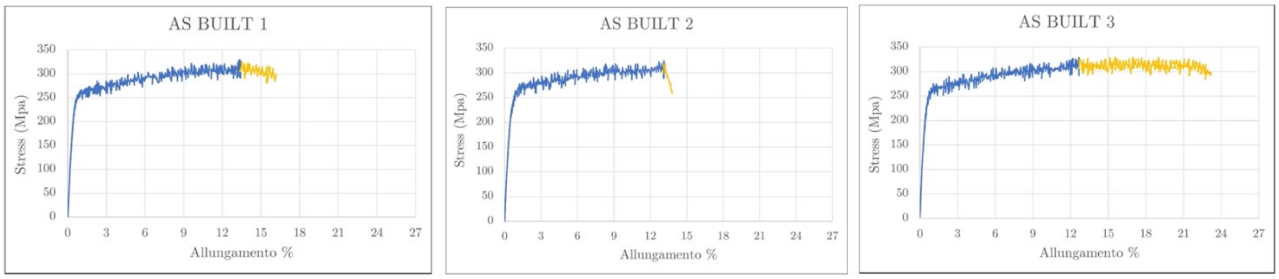

Figure 29 Stress - % El graphs of the as-built specimens

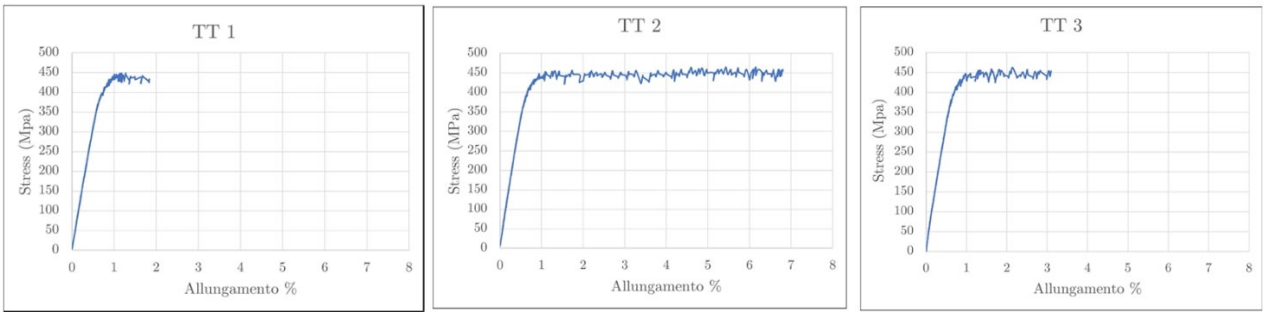

Figure 30 Stress - % El graphs of the heat-treated specimens

The values of the ultimate tensile strength and the yield strength do not differ much from the values of Table 6. Hence the samples analyzed have a good static behaviour. However, the percent elongation is significantly lower.

3.2.4 Optical Microscope Microstructure Analysis

Two samples - one HT and one AB - have received metallographic preparation before the microscope analysis.

Using the cut-off machine Remet TR 60, two sections were created for the samples: one parallel to the printing plane and the other along the rising direction.

The Remet IPA 30 hot mounting press was then used to submerge the samples in a black phenolic resin. Using abrasive paper and specific lapping wheels, the samples were ultimately polished using a Remet LS 1 polishing machine.

Following this procedure, a Nikon microscope was used to investigate the structural defects and take pictures of the sample surfaces at various magnifications.

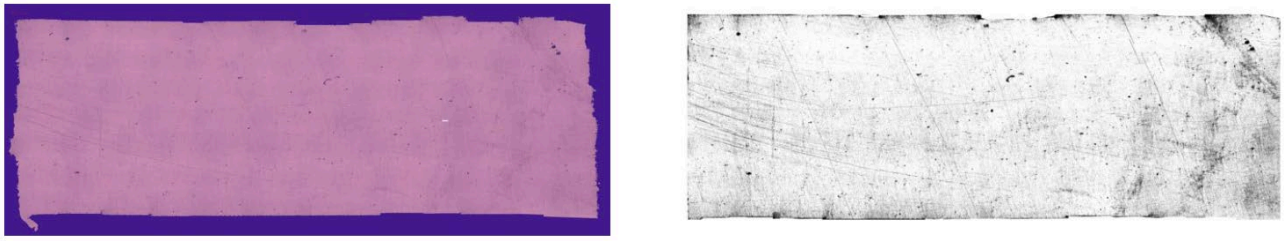

Figure 31 Image of the AB samples along the printing direction taken from the microscope

3.2.5 Microstructure Analysis

The samples' microstructures in the two separate directions were examined by subjecting them to an etching of the Keller type for 20 seconds and then using a Nikon microscope to take images of them at various magnifications. The photos that were taken are shown below.

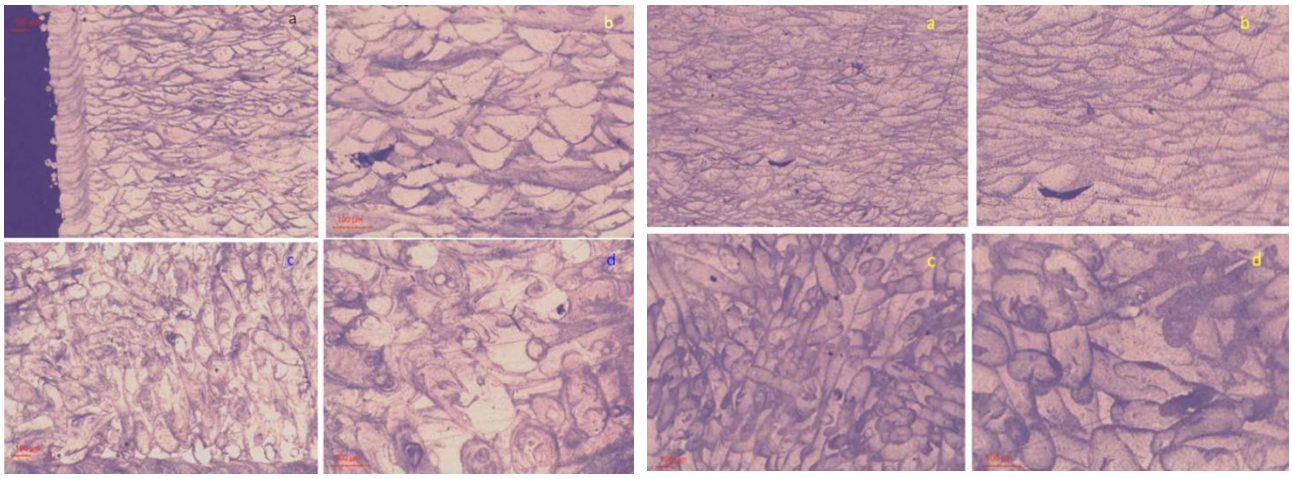

Figure 32 Longitudinal sections (a,b) and transversal sections (c,d) of the AB sample (left) and of the HT sample (right)

The melting pools that form during the L-PBF printing process are clearly visible along the printing path. These are entirely columnar at the edges, but because of the laser's rotation after each layer is printed, they overlap and have a fish-scale appearance in the remaining part of the section [28].

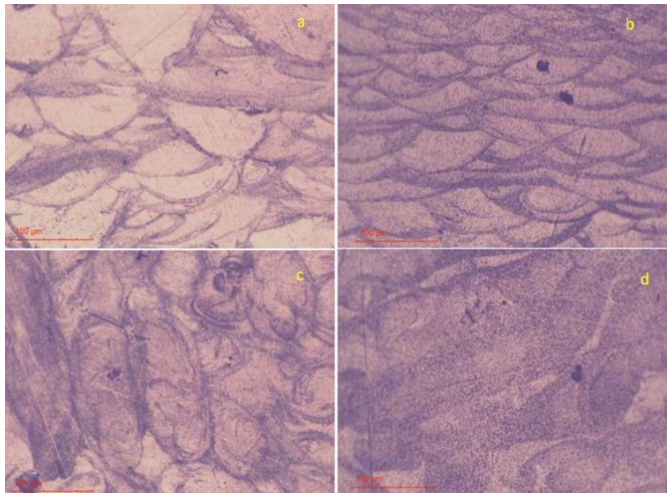

Figure 33 Microstructure comparison between the AB samples and the HT samples

The heat-treated samples may be easily identified due to the presence of precipitates, which are displayed as black dots in Figure 33.

3.2.6 Hardness Analysis

Vickers hardness was determined by taking prints with a 200 gf load for 15 seconds and spacing them 300 μm apart using the REMET HX-1000 durometer. The hardness of the material can be determined by measuring the diagonal of the rhomboidal prints generated by the Vickers durometers. Eight prints of the sample were made in the y direction and eight prints in the x direction.

The hardness value was determined with an average of the results obtained from the two types of tests, which produced the following data:

	Average hardness AB		Average hardness HT	
Section 1	107.7	HV 0.2	169.5	HV 0.2
Section 2	105.1	HV 0.2	175.8	HV 0.2

Table 9 Average Hardnesses of as-built and heat-treated coupons

The hardness in the HT samples has significantly increased.

3.2.7 Static Analysis Results

The difference in values between the HT and AB samples, as shown in Table 8, is due to the presence of Al_3(Sc, Zr) precipitates that result from the thermal treatment. The precipitates cause the sample to become more brittle by decreasing elongation, but they also allow the UTS to increase by about 30%.

However, the microstructure remained unchanged as a result of the heat treatment. The temperature of 325°C during treatment is optimal for precipitation within the compounds, as it does not cause excessive ageing or encourage grain growth.

Additionally, the precipitates increased the material's hardness by about 40%.

The microstructural investigation indicates that the structure of the sample replicates fish scales when cut along the printing direction. This is the outcome of the process of additive manufacturing.

When compared to other alloys, Scalmalloy has fewer defects in terms of porosity [28].

4. Fatigue Analysis in Literature

The literature reviewed is based on the study 'Fatigue properties of Scalmalloy processed by laser powder bed fusion in as-built, chemically and conventionally machined surface condition' [29].

4.1 Printing layout of the coupons

The coupons were built using an EOS M400-1 system, with a layer thickness of 60 µm and in a N_2 atmosphere. Layer by layer, a 67-degree rotation was applied to the stripe pattern created by the laser scanning. To build as-built surfaces with varying initial roughness, samples were created both with and without contour scanning around hatch fields.

The coupons had three different sizes: size A coupons had a cross-sectional area of 12.5 mm^2, size B coupons with 25 mm^2 and size C coupons with 50 mm^2. A 0.5 mm offset was added to the net shape geometries for the samples that had subtractive surface treatments.

4.2 Chemical composition and heat treatment

The chemical composition of the powder and the samples is shown in Table 10.

	Mg	Sc	Zr	Mn	Fe	Others	Al
Powder	4.77	0.78	0.27	0.51	0.12	< 0.06	Bal.
Samples	4.06 ± 0.10	0.75 ± 0.02	0.25	0.49	0.12	< 0.06	Bal.

Table 10 Chemical composition of the coupons [29]

There is an obvious 15% magnesium loss in the chemical composition of the samples. This loss results from low-boiling-point components evaporating due to the high operating temperatures during the LPBF process.

Heat treatment (HT) was performed for two hours at 325 °C in air atmosphere, combining age/precipitation hardening and stress release treatment. For the fatigue samples, hot isostatic pressing (HIP) at 325 °C for two hours under 1000 bar was the second heat treatment step. The best ageing treatment for the Scalmalloy is to combine the heat treatments at 325 °C for four hours, which will result in significant precipitation of Al_3Sc precipitates without over-ageing the material.

The closed porosity of the fatigue coupons was decreased using the HIP process. Evaluating the influence of the surface on fatigue behaviour was the primary objective of these studies. Maximum density was the goal to prevent interior pores from controlling the fatigue fracture behaviour rather than the surface.

Four distinct surface conditions were investigated in the fatigue tests. There were two conditions with as-built surface: "as-hatched," without a contour scan (AH), and "as-built," which had a contour scan

(abbreviated AB). The other two surface conditions were: chemically milled (CM) and mechanically machined (MM). The fatigue samples were machined in compliance with DIN EN 6072.

4.3 Density

Density was determined on crosscut section micrographs and via the Archimedes method. The crosscuts underwent embedding, and SiC paper grinding, and were polished with diamond suspension up to 1 µm. A Keyence VHX-5000 digital microscope was used to take micrographs. A part of the hot isostatically pressed fatigue samples was subjected to X-ray micro-tomography. The techniques showed similar results.

After the SLM process, the coupons' initial density was already high, roughly 99.8%. The density level remained unchanged after the heat treatment for ageing and stress alleviation. The density was raised to around 99.9% via the HIP procedure.

	Archimedes method		Micrographs of crosscut sections	
	relative density	relative porosity	relative density	relative porosity
no heat treatment	99.83 ± 0.01%	0.17 ± 0.01%	99.78 ± 0.12%	0.22 ± 0.12%
heat treated	99.80 ± 0.05%	0.20 ± 0.05%	99.77 ± 0.14%	0.23 ± 0.14%
heat treated + HIP	99.92 ± 0.07%	0.08 ± 0.07%	99.96 ± 0.02%	0.04 ± 0.02%

Table 11 Relative density and porosity measured with two different methods [29]

2.678 g/cm^3 was the theoretical density for Scalmalloy used to calculate the relative density.

The resolution limit of the digital microscope employed in the cross-cut density measurements caused porosities with a diameter smaller than 10 µm to be excluded. Using X-ray microtomography, the low porosity found in density measurements was verified. A minimum resolution of 15 µm voxel size was set. This indicates that porosity smaller than 2-3 voxels (<45 µm) is difficult to find using these techniques. When these results are combined with the crosscut section results, it can be concluded that the remaining 0.04-0.08% porosity is mainly constituted by pores smaller than 30 µm in diameter.

4.4 Microstructure

Light optical microscopy was used to evaluate the microstructure on polished and etched crosscut sections. The crosscuts were embedded, ground with SiC paper up to a grit size of 2000 and polished with diamond suspension up to 1 µm.

The etching solution used was specifically made for Scalmalloy and a Keyence VHX-5000 digital microscope was used to take micrographs.

The macroscopic melt pool boundary lines can be seen in Figure 34 at low magnification. The remelted area resulting from the as-built samples' contour scan can be easily identified as a 200–400 µm surface layer.

When the boundaries of the overlapping melt pools cut perpendicular to the build direction, they resemble fish scales. These melt pools exhibit a bright core and a dark shell at higher magnifications, which correlate to regions of fine grains (FG) on the shell and coarser columnar grains in the core.

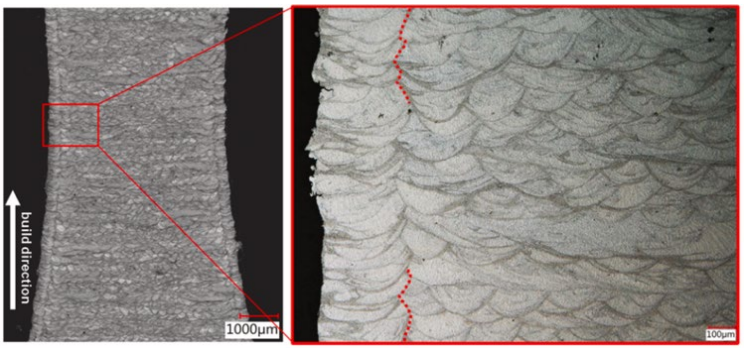

Figure 34 Macrostructure on etched crosscut. The dotted red line shows the visible contour scans on coupons with as-built surfaces [29]

The complex grain structure is seen in SEM images at higher magnifications with BSE contrast and EBSD mappings (Figure 36). The orientation of the coarser columnar grains in the core is in line with the direction of the thermal gradient that leads to the melt pool's centre.

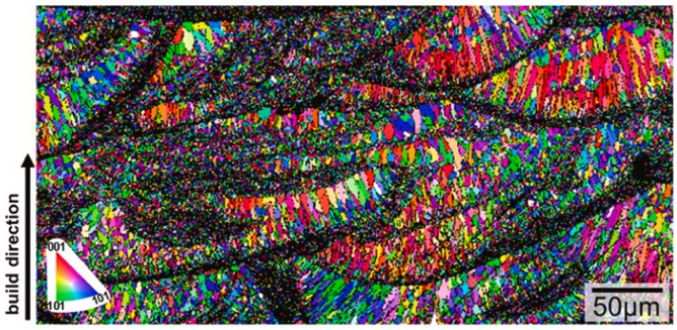

Figure 35 SEM image of overlapping melt pool lines with coarse-grained coloured areas and darker fine-grained areas

The anisotropic mechanical properties of Scalmalloy are a result of fine-grain regions that mostly display equiaxed grains with no preferred direction.

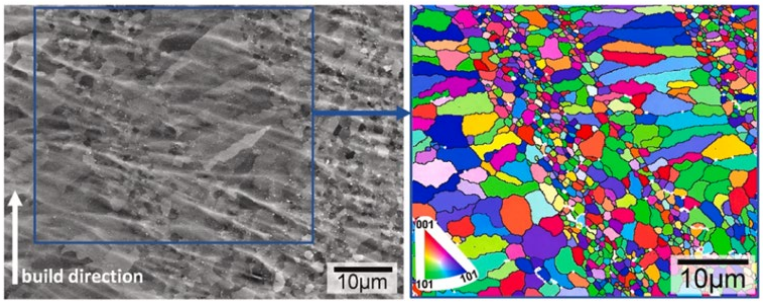

Figure 36 Bimodal microstructure with fine grain (FG) and coarse grain (CG) areas under BSE-contrast and the associated EBSD-mapping

These SEM analyses revealed no evidence of a change in the microstructure following the application of heat treatment and the HIP process. During solidification, heterogeneous nucleation led to the formation of fine grains, which were primarily Al_3Sc and Al-Mg-oxide particles detected on grain

borders. Moreover, during the heat treatments, these particles prevent grain growth and preserve the grain structure [30].

The uniform intragranular precipitation of nanometer-sized Al_3Sc particles from the oversaturated Al matrix is the main result of the heat treatment. The material's hardness is primarily determined by these Al_3Sc precipitates.

4.5 Tensile test

Following DIN EN ISO 6892, quasi-static tensile tests were conducted. A speed of 1 mm/min was used to conduct strain-controlled tensile tests. Testing was done on machined coupons under all three heat treatment conditions (HT, HIP, and NO). For each condition, five samples were examined and averaged.

Figure 37 shows the stress-strain curves for each heat treatment. It is evident how the heat treatment affected the tensile testing. For heat-treated samples, the elongation at break decreased by 30-40% but the ultimate tensile strength increased by about 40%. The strength level of hipped samples and heat-treated samples is the same. The HIP treatment seems to improve only the elongation at break. In the plastic deformation region of not heat-treated coupons, a serrated flow behaviour was noted.

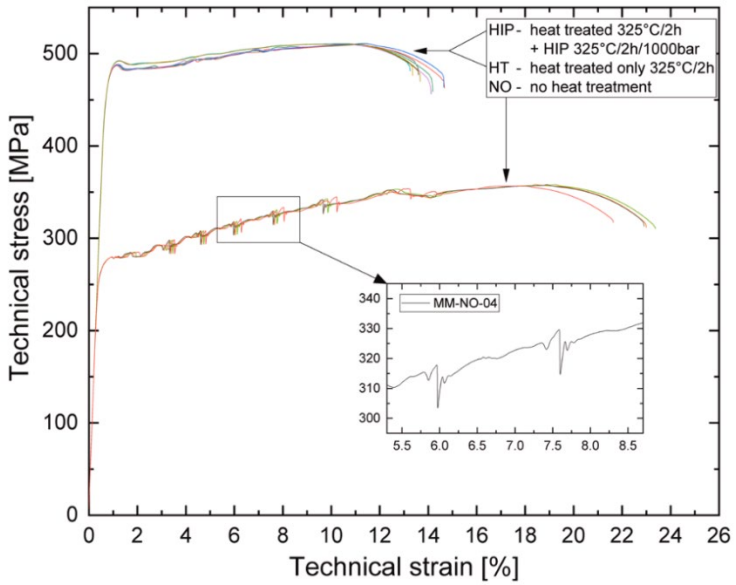

Figure 37 Technical strain-stress curves for machined as-processed, heat-treated, and hipped coupons

In Table 12, all obtained strength, Young's modulus and ductility values are displayed.

	Young's modulus E [GPa]	Yield strength Rp0.2 [MPa]	Ultimate tensile strength Rm [MPa]	Elongation at break A [%]	Necking /reduction of area Z [%]
MM NO	70.7 ± 0.1	270.0 ± 0.4	357.9 ± 0.8	22.9 ± 2.2	42.9 ± 2.5
MM HT	71.3 ± 0.3	476.9 ± 0.3	510.8 ± 0.1	13.4 ± 0.3	25.9 ± 1.4
MM HIP	71.5 ± 0.3	475.4 ± 0.5	510.1 ± 0.5	14.2 ± 0.4	26.6 ± 1.5

Table 12 Data obtained from tensile testing. The values of 5 coupons were averaged

The heat treatment reduces ductility and increases the strength of the consolidated material by the precipitation of the nanometer-sized Al_3Sc particles. Although HIP treatment does not significantly increase strength, it does provide a slight increase in ductility, most likely because of the decreased porosity.

It is possible to compare the results with those of 3.2.3 and observe that although the elongation has considerably lower values, the tensile strength is lower but does not differ significantly.

4.6 Roughness

Under DIN EN ISO 4288, surface roughness was measured using a tactile profilometer Waveline T8000. On the fatigue coupon heads, 12 automated roughness measurements (as on a clock) were performed for each coupon. Using the related software EVOVIS, the roughness parameter Ra was found from the line profiles in line with DIN EN ISO 4287. Each coupon's twelve roughness measurements were averaged.

The surface states are ranked in the order AH>AB>CM>MM by the mean roughness parameter Ra, calculated with an arithmetic mean, which has an inverse correlation to their fatigue performance. The required surface finishing from DIN EN 6072 with Ra < 0.8 µm can be observed in machined MM-coupons. The surface roughness was successfully reduced by chemical milling, but the AB and AH roughness values are quite similar.

Average surface roughness (from 468 measurements)	Surface modification			
	AB	AH	CM	MM
Ra[µm]	20.6 ± 6.3	22.7 ± 2.7	15.3 ± 2.2	0.4 ± 0.1

Table 13 Average surface roughness

4.7 Fatigue Test

In Figure 38 all the data from the fatigue testing are presented.

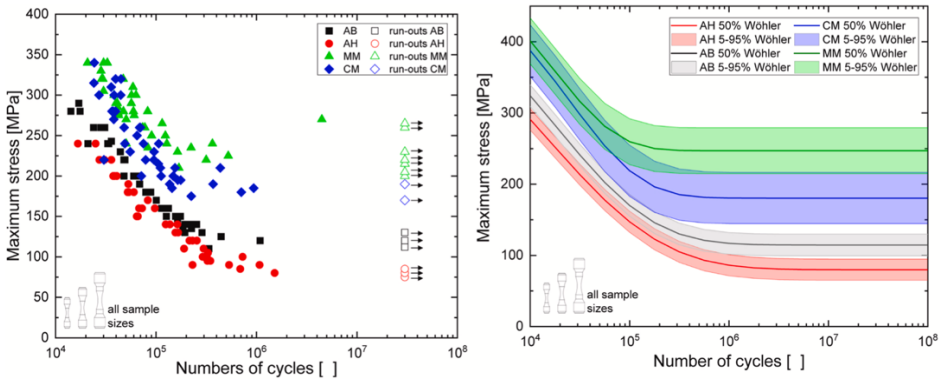

Figure 38 S-N curves for all the coupons (left) and calculated 5–50% and 95% Wöhler-curves (right)

The coupons with the two as-built surface states (AB and AH) exhibit a significantly reduced fatigue strength in both the LCF range (less than 100,000 cycles) and the HCF range (more than 100,000

cycles), as predicted. Aluminum materials usually lack an authentic fatigue strength. For this reason, the technical fatigue strength is determined by the run-outs at 3.0×10^7 cycles.

Table 14 provides the computed notch factors K_f along with a summary of the technical fatigue strength for all surface modifications and sample sizes.

	AH (as-hatched)	AB (as-built)	CM (chemically milled)	MM (mechanically machined)
Sample size A	80 MPa	120 MPa	170 MPa	215 MPa
Sample size B	85 MPa	130 MPa	170 MPa	265 MPa
Sample size C	85 MPa	112 MPa	190 MPa	230 MPa
Fatigue notch factor K_f	2.5 – 3.3	1.7 – 2.3	1.1 – 1.6	1

Table 14 Technical fatigue strength for all surface modifications and sample sizes. Fatigue notch factor K_f is shown

Compared to the AH specimens without a contour scan, the AB specimens with a contour scan have a strength level that is 30 - 40 MPa higher. This is explained by the morphology of the surface.

Chemical milling proved to be an effective surface treatment, as seen by the CM coupons' significantly higher fatigue strength (30 - 70%) when compared to the AB samples. Given the higher roughness on the CM surfaces, fatigue strength values of 64 - 83% of the MM samples are significant when comparing the CM to the MM samples.

The fatigue strength up to 265 MPa (MM samples) cannot easily be compared with values from the literature because only three other publications have published fatigue values for Scalmalloy with R=0.1.

The two as-built surfaces, AB and AH, have substantially smaller scattering widths of strength values than the modified surfaces, CM and MM. In as-built surfaces, fracture often results from surface irregularities, such as notches and depressions in the melt surface, semi-molten powder particles, melt splatter, inclusions, and impurities. The fracture-inducing defect is primarily responsible for the discrepancy. In machined and post-processed coupons, volume defects in the surface and sub-surface regions, such as gas pores, LoF defects, inclusions, and impurities, are the main causes of fracture origin. In samples made by additive manufacturing, the size of volume defects varies substantially and is influenced by many processing parameters. In post-processed additively made specimens, this variance in volume defect size causes a higher scatter of the dynamic strength, particularly in the HCF region.

The Kitagawa-Takahashi diagrams can be used to explain how the dynamic strength depends on the defect size from the perspective of fracture mechanics. In this context, the defects are interpreted as short cracks that follow the √area-concept proposed by Murakami and Endo [31]. SEM pictures

obtained from the fracture surface are used to calculate the defect size of the fracture-inducing defects, which are then displayed later in 4.8.

4.7.1 Coupon size independence

More investigations were conducted, regarding coupon size independence. There is no noticeable size dependence on the fatigue results for the AB and AH specimens.

In Figure 39, the four surface modifications are each plotted independently, without the 5% and 95% Wöhler limits, allowing the comparison of data across the different specimens. There is no apparent size dependence on the fatigue results for the AB and AH specimens. The three specimen sizes' Wöhler curves overlap in all areas, and there is very little scatter in the individual data points following the Wöhler curves.

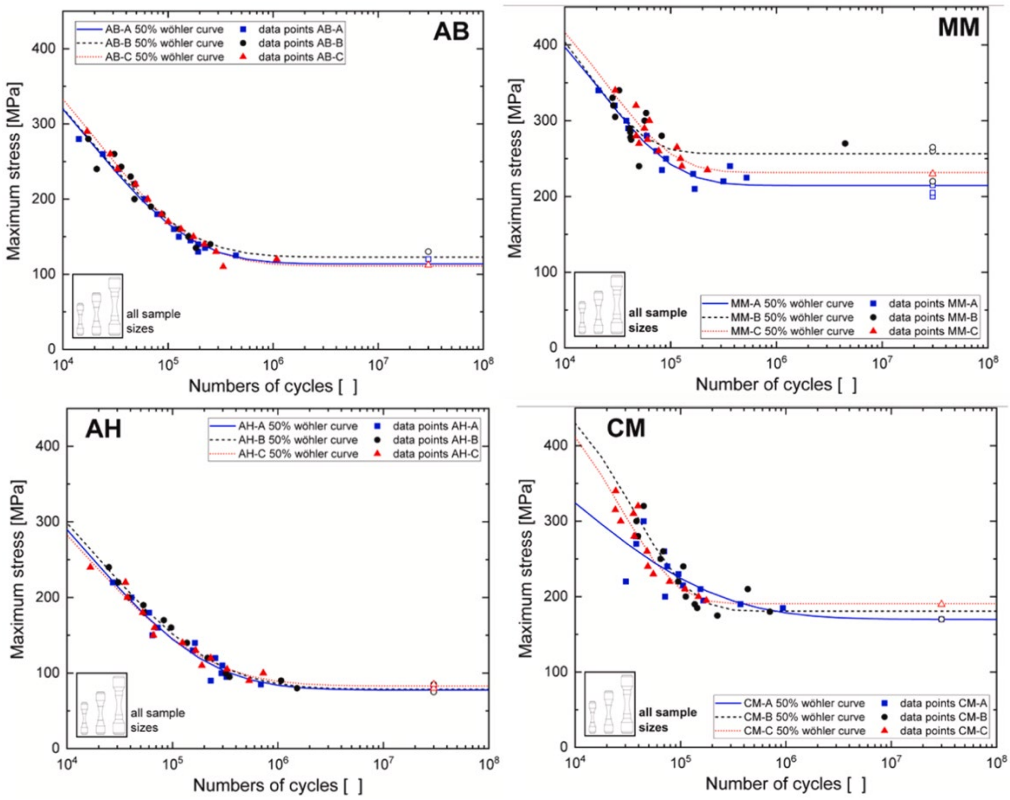

Figure 39 Fatigue results of all 3 sample sizes divided by their surface condition with the calculated 50%-Wöhler-curves. Data points without filling are run-outs at 3.0 x 10^7 cycles

The two Wöhler curves for samples CM-B and CM-C have a significant amount of overlap. There is not an apparent size-dependent trend. The Wöhler curve for specimens CM-A in the LCF-regime is flatter, not because of a systematic size dependence, but rather because of the two outliers at 30,000 and 70,000 cycles. Similar to the MM specimens, certain defects can be linked to the fracture origin of the CM specimens.

The fatigue performance and scatter are determined by the dimensions of these defects, particularly in the HCF range. These imperfections are individual etching pits on the CM surfaces. The technical

fatigue strength scatters most for the machined MM specimens. The HCF range is where most of the variations in the Wöhler curves can be found. For every coupon size, the LCF range yields consistent results with an acceptable scattering resulting from scatter in the size of the fracture-inducing defects. These defects include spherical oxide particles, material/microstructure inhomogeneities, and LoF defects for the MM samples.

4.8 Fractography

Every specimen had fracture initiation sites at their surfaces. Consequently, the AB and AH coupons failed at the rough surface defects, which were usually the notches caused by adhering particles, roughness valleys, and irregularities of the melt surface. The semicircular etch pits, or more precisely, the notch base of these etch pits, were where the CM specimens failed. Little defects on the specimen surface caused the MM specimens to fail.

Table 15 provides an overview of the specimens examined, including the number of fracture initiation sites, their location, and the typical defect sizes utilizing Murakami's √area parameter.

Surface modification Sample size	Investigated samples SEM	Fracture initiation location	Number of fracture initiation sites (isolated cases)	Typical $\sqrt{area}$ defect size [µm]
AB-A	6/13	at the surface	3–13	N.A.
AB-B	5/13	at the surface	2–13	N.A.
AB-C	6/13	at the surface	2–22	N.A.
AH-A	8/13	at the surface	2–5	N.A.
AH-B	4/13	at the surface	3–6	N.A.
AH-C	6/13	at the surface	3–6	N.A.
CM-A	9/13	at the surface	1 (2,2,2)	150 ± 124
CM-B	7/13	at the surface	1 (2)	152 ± 136
CM-C	6/13	at the surface	1 (2,4)	197 ± 116
MM-A	9/13	at the surface	1 (2)	31 ± 22
MM-B	8/13	at the surface	1 (2)	39 ± 35
MM-C	8/13	at the surface	1	43 ± 30

Table 15 Data regarding the coupons analyzed: number of fracture initiation location sites, their location and the typical √area defect size

Every examined specimen, both as-built and as-hatched, has two or more locations where the fracture begins.

The stress on the remaining cross-section increases once the specimen enters the stable crack growth phase and a first crack front has formed. An additional crack at another defect with a greater stress intensity factor is more likely to start the higher the applied stress. More fracture initiation sites were often discovered on the fracture surfaces of the AB and AH specimens at higher test stresses. But there's also a little chance that cracks could initiate simultaneously at plenty of defect locations, particularly on highly irregular as-built surfaces. Because of this, for some samples, it can be hard to determine the main defect that gave rise to the initial crack. Furthermore, it is challenging to

distinguish the precise contours and extent of the defects in these samples from the remaining part of the asymmetrically shaped as-built surface. As a result, it is challenging to determine the precise defect size for the AB and AH specimens that caused the specimens to fail.

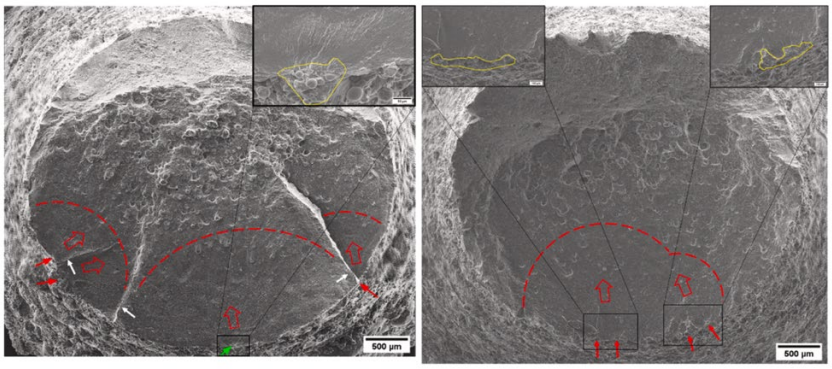

Figure 40 Four fracture initiation sites are present on the fracture surfaces of the AB specimen (left) and the AH specimen (right). Where stable crack growth has occurred, the primary and secondary crack growth areas are shown by the red dashed arcs. The region of unstable crack growth and ductile residual fracture is shown above these arcs

AB and AH specimens with several fracture initiation sites are shown in Figure 40. The semicircular-shaped stable crack growth zones, represented by dashed lines, are visible and have an extremely smooth surface originating from the primary and secondary defects. Unstable crack growth develops when the combined fatigue crack area reaches a critical size. The regions where unstable crack growth is occurring are considerably rougher and visually distinguished from those where stable crack growth is occurring. In unstable crack growth, the crack reaches a critical area when the specimen's remaining cross-section can no longer bear the applied stress and breaks in a ductile way.

Extreme value statistics can be used to explain the trend of increasing average defect size with an increasing sample size. The probability of discovering a larger defect increases with the volume tested.

There is also a modest sample size dependence that is observable. Size A samples have the smallest defect sizes, particularly on MM surface conditions, while size C and B samples typically have the largest defects. Except for a few individual size A samples that had larger defects and were also in charge of the bigger scattering in the fatigue performance, the same is true for the CM surface condition.

These largest extreme value statistics can be used to identify the largest probable defect in a bigger sample or component volume.

Romano et al. [32] contended that fatigue specimen fracture only identifies the biggest defect in the surface area of the specimens rather than across the volume since the defects are all found at the specimen surface.

4.9 Conclusions

From [29] different outcomes were found. The HIP treatment was effective in reaching the highest density and allowed for a discussion of the surface's influence without the sub-surface porosity playing a major role. AH < AB < CM < MM was the sequence in which the fatigue strength of the four surface alterations occurred. As compared to samples without contour scans (AH), those with contour scans considerably improve the fatigue strength of samples in the as-built surface condition (AB).

When adequate material removal and maximum density are guaranteed, post-processing (CM and MM) the surface significantly improves the dynamic strength (in comparison to as-built surfaces). Therefore, chemical milling is effective in increasing fatigue performance even in cases where roughness reduction is restricted. The size of the fracture-inducing defects dominates fatigue behaviour and is independent of sample size. Every sample, both unprocessed and processed, failed from the surface.

Fractographic analysis revealed that the rough as-built surface defects, which were mostly adherent particles, irregularities of the melt surface, and notches of roughness valleys, were the reason why the AB and AH samples failed. The semicircular etch pits on the surface were where the CM samples failed. MM samples failed at the small defects (LoF defects, oxide inclusions, material, and microstructure inhomogeneities) placed on the surface.

While CM and MM samples usually have a single defect that causes the fracture, all broken AB and AH samples showed several fracture initiation sites. The largest impact on the fatigue performance of the MM and CM samples is caused by the size of these fracture-inducing defects.

5. Fatigue Analysis

Following the literature review, an experimental campaign was carried out on 20 coupons. A fatigue test and a metallographic characterization have been conducted in this campaign. Afterwards, the obtained data were compared with the results gathered from the literature.

5.1 Coupons' shape

The coupons used for this analysis were printed following the same technique used for the static analysis, as seen in 3.2.1. The only substantial difference is in the shape of the coupons. The coupons used for the fatigue analyses have a cylindrical shape.

Figure 41 Cylindrical coupon used in fatigue analysis

The coupons, in their central resistant section, were treated with a lathe after printing, to remove the roughness generated by the additive printing procedure [33].

5.2 Coupon inspection

The analysis was conducted on 20 coupons. Different inspections have been conducted before the fatigue tests.

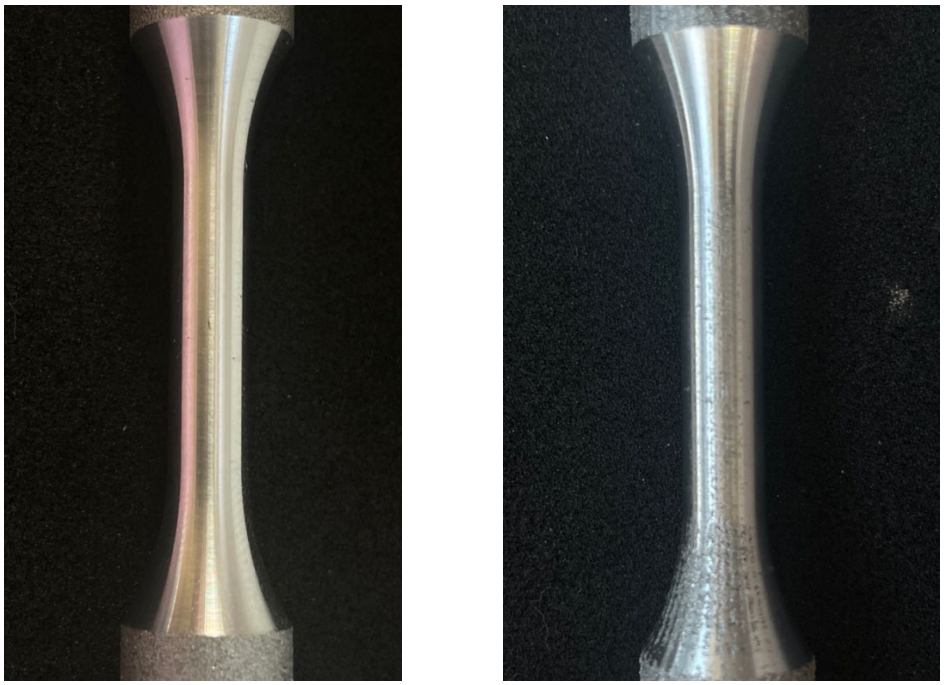

Figure 42 Photos of coupons 1 (left) and 4 (right)

5.2.1 Stereoscope analysis

Several photos have been taken with the Carl Zeiss Stereo Microscope Stemi 305 (Figure 43).

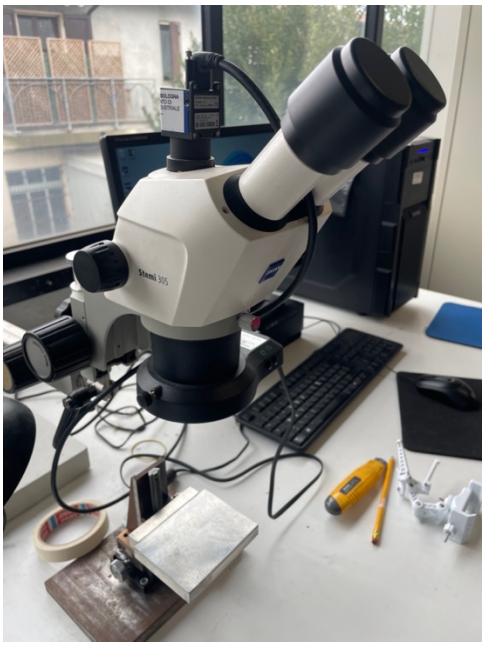

Figure 43 Carl Zeiss Stereo Microscope

Each coupon has been observed with various enlargements and some defects and irregularities were detected on their surface. The roughness of these coupons is evident, resulting from the additive manufacturing printing.

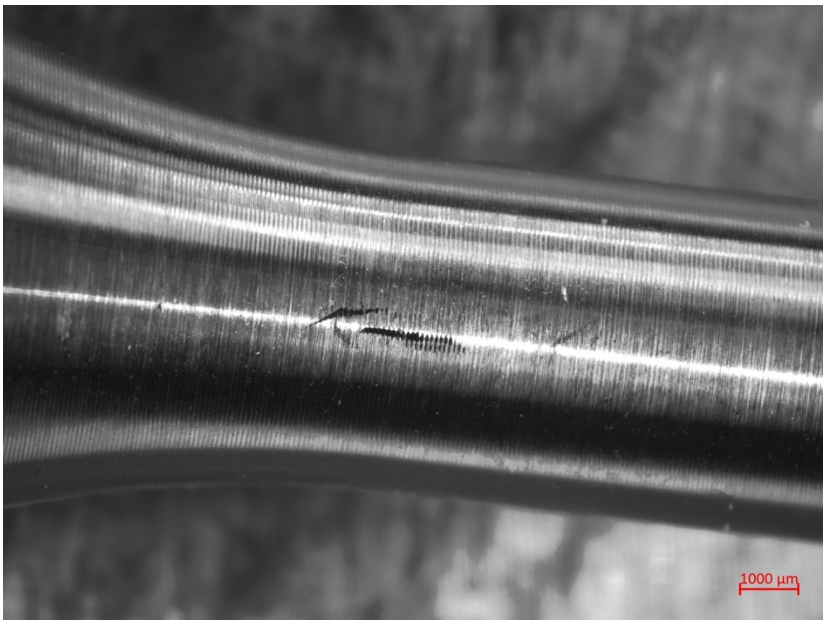

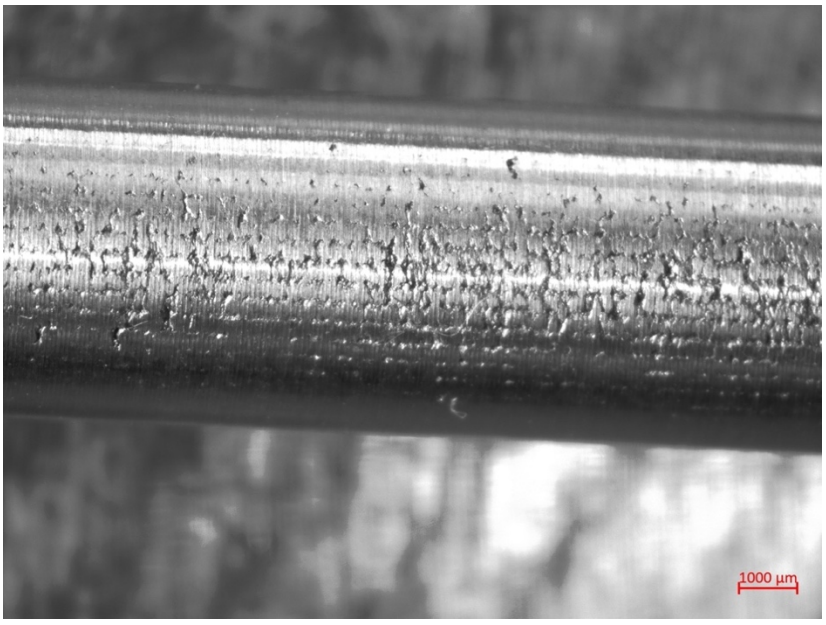

Figure 44 Photos obtained with the stereo microscope of coupon 1 (above) and 4 (below)

Some coupons show a smoother surface, with only a few defects, while others have a more rough surface, which can be seen in Figure 44.

The presence of defects directly on the surface of the coupons is evident.

5.2.2 Diameter Analysis

The diameter of each coupon has been computed with the micrometre Mitutoyo (Figure 45).

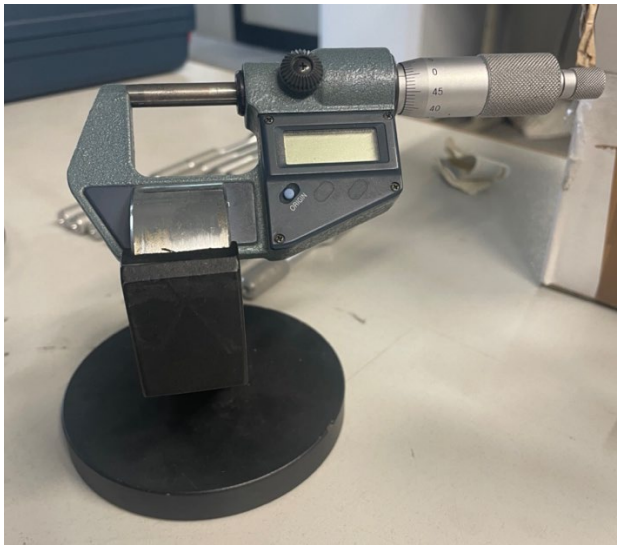

Figure 45 Mitutoyo micrometer

For each coupon 4 measurements were taken, 2 measurements in 2 different points of the resistant section, in 2 different orthogonal directions (almost 180° apart one from the other). The final diameter has been obtained by calculating the average. The results are listed in Table 16.

Coupon	D1_1 [mm]	D1_2 [mm]	D2_1 [mm]	D2_2 [mm]	D_fin [mm]
1	5,799	5,805	5,791	5,791	**5,797**
2	5,822	5,811	5,792	5,788	**5,803**
3	5,791	5,791	5,799	5,799	**5,795**
4	5,796	5,798	5,790	5,789	**5,793**
5	5,783	5,788	5,795	5,792	**5,790**
6	5,795	5,798	5,789	5,788	**5,793**
7	5,793	5,790	5,799	5,796	**5,795**
8	5,798	5,798	5,790	5,791	**5,794**
9	5,687	5,674	5,694	5,700	**5,689**
10	5,798	5,798	5,790	5,791	**5,794**
11	5,794	5,794	5,800	5,800	**5,797**
12	5,794	5,795	5,788	5,789	**5,792**
13	5,684	5,689	5,693	5,692	**5,690**
14	5,797	5,797	5,789	5,788	**5,793**
15	5,893	5,845	5,901	5,848	**5,872**
16	5,789	5,787	5,793	5,793	**5,791**
17	5,785	5,790	5,796	5,795	**5,792**
18	5,795	5,796	5,788	5,789	**5,792**
19	5,787	5,789	5,795	5,788	**5,790**
20	5,798	5,800	5,791	5,792	**5,795**

Table 16 Diameter computation for each coupon

5.2.3 Roughness analysis

The roughness of each coupon has been measured with a roughness tester Alpa metrology RT-10G (Figure 46).

Figure 46 Roughness tester Alpa metrology RT-10G

3 measurements have been taken for each coupon, on the cylinder generator and 120° apart. The final roughness has been calculated with an average, and it can be seen in Table 17. The first roughness measurement of coupon 9 is shown in Figure 47.

Coupon	Ra_1 [µm]	Ra_2 [µm]	Ra_3 [µm]	Ra_fin [µm]
1	0,258	0,329	0,329	**0,305**
2	0,521	0,366	0,371	**0,419**
3	0,216	0,215	0,229	**0,220**
4	0,530	0,537	2,142	**1,070**
5	0,380	0,367	0,349	**0,365**
6	0,378	0,425	0,286	**0,363**
7	0,351	0,561	0,490	**0,467**
8	0,419	0,785	0,409	**0,538**
9	0,418	0,333	0,445	**0,399**
10	0,596	0,581	0,590	**0,589**
11	0,326	0,396	0,378	**0,367**
12	0,381	0,448	1,103	**0,644**
13	1,502	0,610	0,652	**0,921**
14	0,464	0,540	0,420	**0,475**
15	0,249	0,278	0,640	**0,389**
16	0,984	0,549	0,520	**0,684**
17	0,450	0,536	0,594	**0,527**
18	0,412	0,494	0,482	**0,463**
19	0,195	0,244	0,184	**0,208**
20	0,546	0,637	0,628	**0,604**

Table 17 Roughness measurements for each coupon

A roughness average value is computed and is equal to 0,500 µm. Though not significantly different, it is higher than the value found in the literature, equal to 0,400.

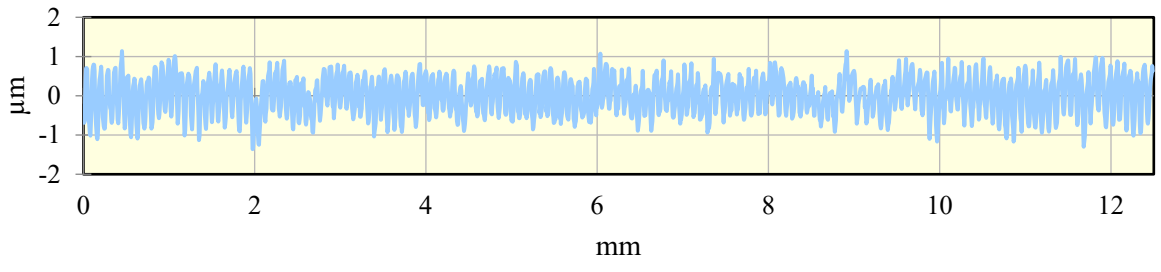

Figure 47 First roughness measurement of coupon 9

5.2.4 Eccentricity

The eccentricity of each coupon has been analyzed with an Accud comparator (Figure 48).

Figure 48 Accud comparator

The measurements have been taken after placing the coupons in the rotary bending machine, before starting the fatigue test. The measurements obtained are in Table 18.

Coupon	Eccentricity [mm]
1	0,190
2	0,500
3	0,100
4	0,500
5	0,700
6	0,250
7	0,430
8	0,850
9	0,070
10	0,220
11	0,150
12	0,400
13	0,600
14	0,650
15	0,450
16	0,650
17	0,170
18	0,350
19	0,640
20	0,110

Table 18 Eccentricity measurements for each coupon

Some coupons have a lower eccentricity than the others. This will affect the number of cycles that each coupon will compute during the fatigue testing.

5.3 Fatigue Testing

The fatigue tests were conducted in the ITALSIGMA rotary bending machine (Figure 49).

Figure 49 Rotary bending machine

Every coupon has been placed in the machine and they have been clamped anchoring their grip sections in the two mandrels. The coupons are anchored using two spring collets placed inside the two mandrels.

Each coupon has its different load applied (values in Table 19). The values of the loads are computed with equation (3):

$$Applied\ Load\ [kg] = \frac{2\frac{\pi d^3}{32}\sigma}{gL} \tag{3}$$

where d is the coupon's diameter (mm) found in Table 16, σ is the theoretical stress to be applied (MPa), g is the gravitational acceleration (9.81 m/s^2) and L is equal to 140 mm.

Every load is then settled in the machine and the test can start. The machine speed can be controlled, and it is increased with a potentiometer until it reaches the desired value. The speed is about 3200 rpm for most of the coupon.

Once the machine reaches the desired speed, it is left operating until the coupon breaks. The machine then displays the number of completed cycles which is noted.

The machine rotates the coupons along its axis by applying a specific bending moment to them.

This system can be schematized as a supported isostatic beam with two locations where the load is applied, as shown in Figure 50.

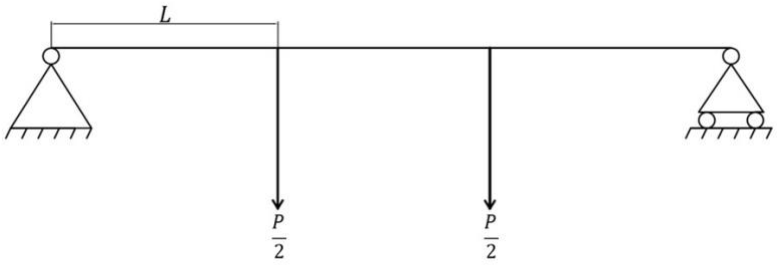

Figure 50 Scheme of a supported isostatic beam.

5.4 Results of the fatigue testing

5 coupons have been tested for 4 different values of the theoretical stress σ. The applied loads have been computed with the equation (3) presented in 5.3. The number of cycles fulfilled by each coupon is displayed in Table 19.

Coupon	σ [MPa]	Applied Load [kg]	Machine speed [rpm]	N
1	300,000	8,350	3200	13467
2	300,000	8,350	3000	11565
3	300,000	8,350	2330	9696
4	250,000	6,950	3200	15161
5	250,000	6,950	3200	22571
6	250,000	6,950	2900	12120
7	200,000	5,550	2400	28700
8	200,000	5,550	3200	34347
9	200,000	5,250	3000	43120
10	200,000	5,550	3000	63328
11	200,000	5,550	3200	64642
12	150,000	4,150	3000	86220
13	150,000	3,950	3200	104565
14	150,000	4,150	2800	63345
15	150,000	4,350	3200	191683
16	150,000	4,150	3200	86884
17	250,000	6,950	3200	15200
18	250,000	6,950	3200	18684
19	300,000	8,350	3200	16116
20	300,000	8,350	3200	11713

Table 19 Theoretical stress σ, applied load, machine speed and number of cycles resulting for each coupon

An arithmetic average has been computed for the number of cycles, for every theoretical stress used and the averages are listed in Table 20.

Average number of cycles	σ [MPa]
12511	300
16747	250
46827	200
106539	150

Table 20 Average number of cycles for each theoretical stress σ

The S-N Wöhler curve can be developed from the data shown in Table 19.

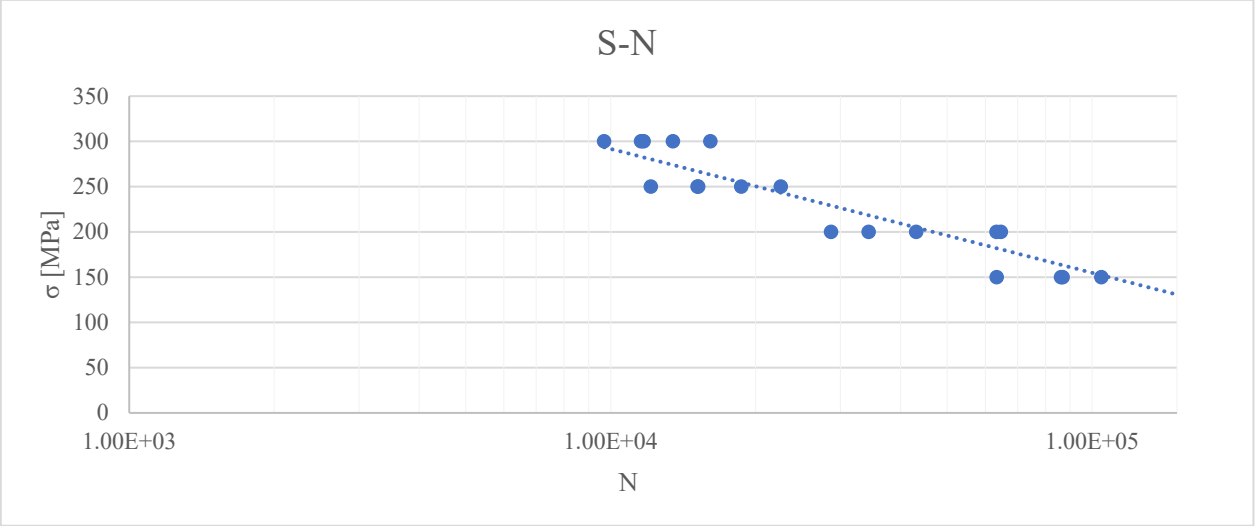

Figure 51 Wöhler curve.

The data obtained showed a discrepancy between the number of cycles obtained experimentally and the ones reviewed in the literature. At high theoretical stress, the coupons encounter failure at low values of N. Also, a wide scatter between the number of cycles of coupons tested at the same theoretical stress has been detected. So, the coupons are not reliable in both low and high values of theoretical stresses.

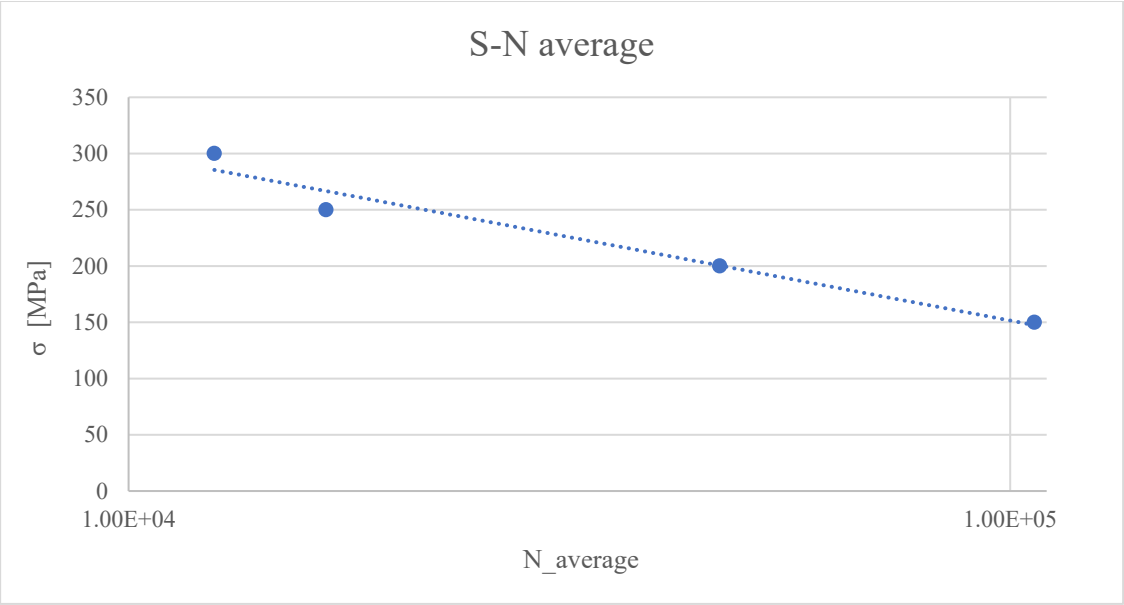

Figure 52 Wöhler curve with average data

It is noticeable that the curves developed in the study presented in 4.7 have an evident change of slope that could not be identified in these curves. Here, there is no horizontal line representative of the horizontal asymptote. This means that these coupons do not guarantee a zone of 'infinite life' below certain values of stress.

The high eccentricity of coupons could be one of the causes for the low resistance to fatigue, but more analysis will be done to understand why the coupons exhibit this behaviour. A metallographic and fractography characterization will be completed.

6. Metallographic Characterization

2 coupons per theoretical stress are going to be analyzed, the coupons that are at the boundaries in each line of the theoretical stresses (the coupon with the lower N and the one with the higher N for the same σ).

Coupons 3 and 19 are the ones investigated for a theoretical stress equal to 300 MPa, for σ = 250 MPa the coupons examined are 5 and 6, 7 and 11 are the ones for σ = 200 MPa and, for the last theoretical stress equal to 150 MPa, the coupons studied are 14 and 15.

6.1 Cutting and hot-pressing processes

Many steps are required to examine the microstructure of the coupons.

Each coupon is now divided into two parts after the failure occurred in the fatigue testing. The part to be wrought is selected arbitrarily and then the Remet TR 60 cut-off machine (Figure 53) will be used to cut it. These instruments are very useful for collecting samples from components of any shape. Rapid, rigorously cold, and deformation-free cutting of any kind of material is possible with the cut-off machine. The gripping system comprises a self-centering, double-clamping vice [34].

Figure 53 Remet TR 60 cut-off machine

The aim is to cut a part of the resistant section and a part of the grip section of the coupon to analyze both. After obtaining the two different parts, they will be inserted together in the hot mounting press

to be embedded with phenolic resins. The hot mounting press used for this analysis is the Remet IPA 30 hot mounting press (Figure 54). Using any kind of thermosetting or thermoplastic resin, the embedding presses produce perfect inclusions of metallographic samples very quickly [35].

Figure 54 Remet IPA 30 hot mounting press

The final sample produced by this technique is shown in Figure 55 and it is evident that the surface is rough.

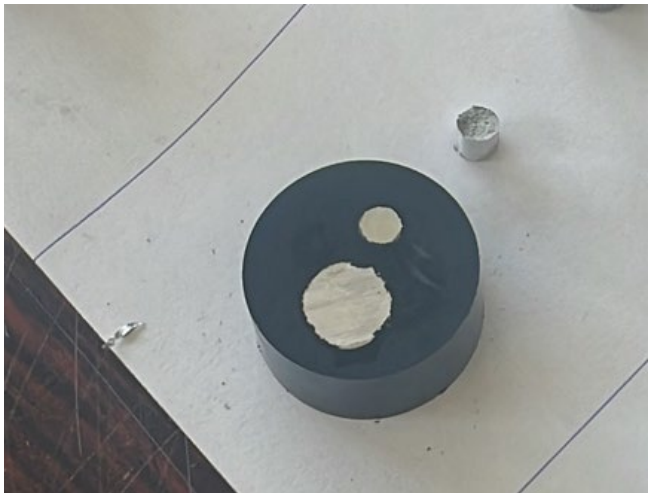

Figure 55 Parts of the resistant and grip section of one coupon embedded with black phenolic resin

6.2 Grinding and polishing processes

The next step is to grind and polish this new component's surface with a Remet LS 1 polishing machine (Figure 56). A rotating plate holds the different cloths, and water flows from the tap, to keep the procedure cold.

Figure 56 Remet LS 1 polishing machine

Grinding is a long process during which different cloths are exchanged among them, one after the other. The purpose of metallographic planar grinding is to make ground surfaces flat and to eliminate roughness from the metallographic cutting process. Material is removed from the surface using abrasive particles with progressively smaller grain sizes until the intended result is achieved [36].

The process consists of different steps during which grinding foils of different grain sizes are substituted. During the grinding process with one foil, several lines appear on the surface of the embedded coupon. When the foil is exchanged and every line of the foil used before is parallel to one another and so when every scratch left by the preceding foil has been removed, the objective is achieved.

Every time the foil is changed, the coupon needs to be turned by 90° to avoid overlapping the cleaning lines with the ones from the previous foil, which will help each cleaning step go more smoothly. The coupon needs to be well-cleaned with water before being transferred to the next foil.

The final step provides polishing the coupons with 3 polishing cloths in gradually finer grain sizes, and alumina suspensions. The process is the same as before and at the end, the coupons are polished, an example can be seen in Figure 57.

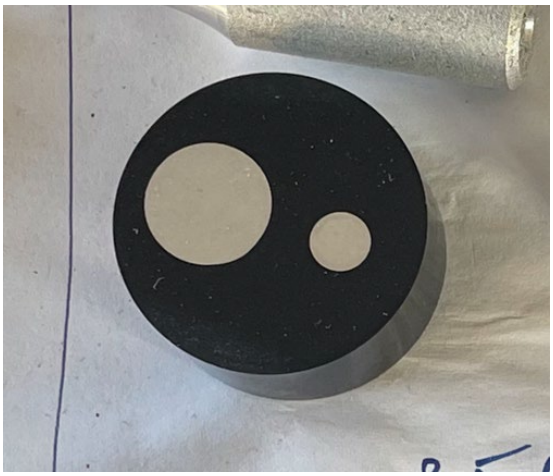

Figure 57 Coupon after polishing process

The last step is to place the coupons in the ultrasonic cleaner, shown in Figure 58, for 5 minutes to clear any potential defect.

Figure 58 Ultrasonic cleaner

6.3 Stereoscope Observations

The coupons are now ready to be observed in detail. The first inspection has been done with the stereoscope of Figure 43 of both the resistant and the grip sections.

In Figure 59 and Figure 60, the sections of coupon 15 are shown. Only a part of the grip section is visible because it could not fit entirely in the shot.

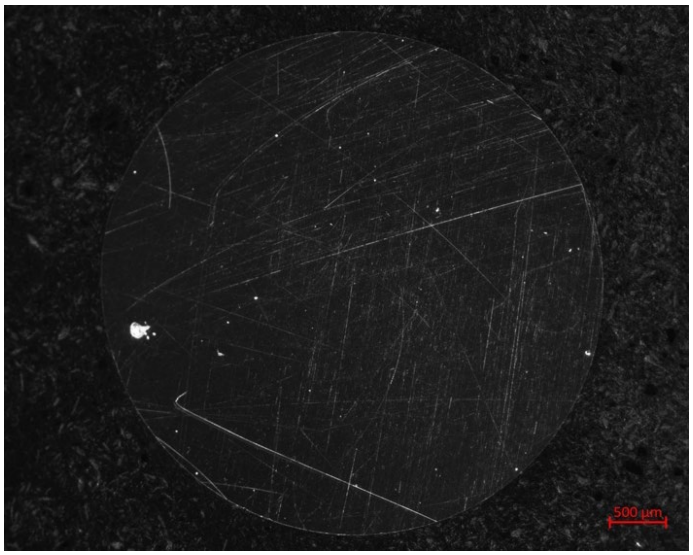

Figure 59 Resistant section of coupon 15

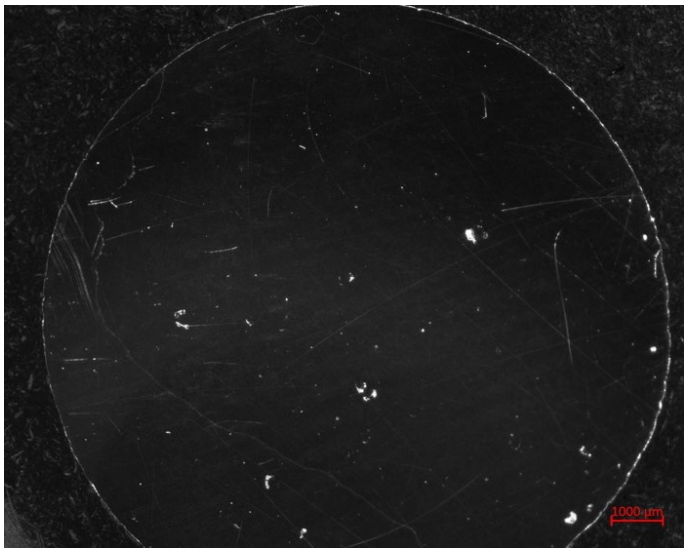

Figure 60 Grip section of coupon 15

In both sections, different defects are visible (mostly in the grip section) and an enlargement of the resistant section is present in Figure 61, in which an evident defect is captured, and it is noticeable that its size is quite big.

Some lines are still visible in the pictures. These are the lines produced in the grinding process, the most difficult to remove.

The defect size is 353,222 µm and comparing it with the defect dimensions listed in Table 15, regarding the study analyzed in Chapter 4, the dimensions are quite bigger. In those defects, the CM coupons presented defects with sizes in a range from 150 µm to 197 µm, and the MM ones have defect sizes in a range from 31 µm to 43 µm.

This difference between the defect sizes can be one of the causes of the behaviour obtained in the fatigue test of the coupons. These defects could promote crack growth inside the coupons.

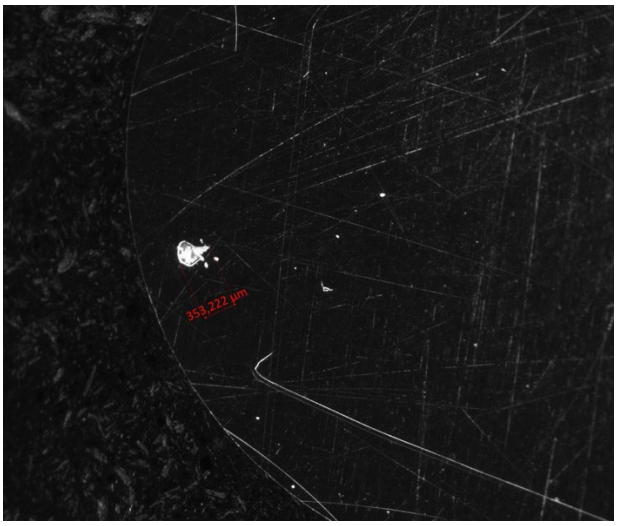

Figure 61 Enlargement of the resistant section with an evident defect

It's important to consider a variety of possible error sources when looking for the right process. One of these sources could be the comet tails which usually occur adjacent to pores, hard phases, and non-metallic inclusions when the section is manually held in only one direction [37]. An example is shown in Figure 62.

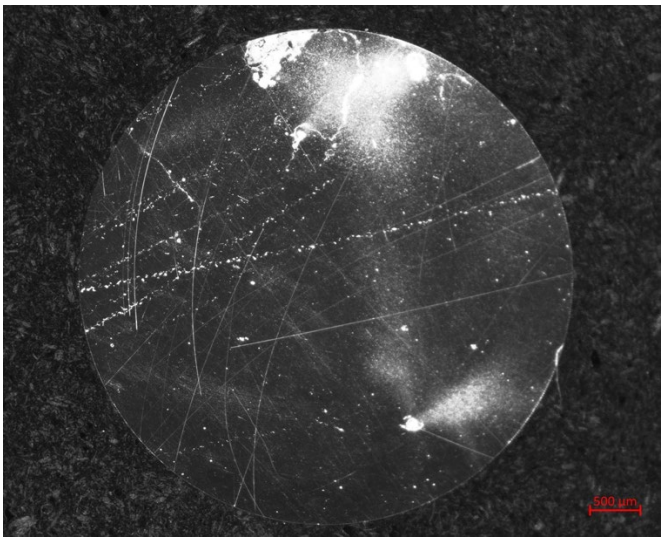

Figure 62 Comet tails in the resistant section of coupon 3

The resistant sections of all the coupons are included in APPENDIX A.

6.4 Microscope Observations

The coupons are then examined using a Nikon microscope (Figure 63).

Figure 63 Nikon optical microscope

Only the resistant section has been analyzed in this inspection, of which a small part is visible (Figure 64).

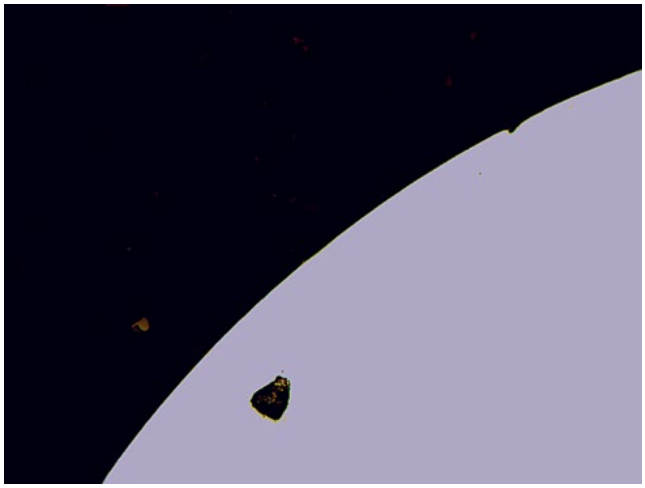

Figure 64 Part of the resistant section of coupon 5 analyzed with the microscope.

The entire resistant section can be identified by stitching together all the portions of the resistant section. The result can be seen in Figure 65. Stitching all the parts of the resistant sections of all the coupons helps in the calculation of the porosity.

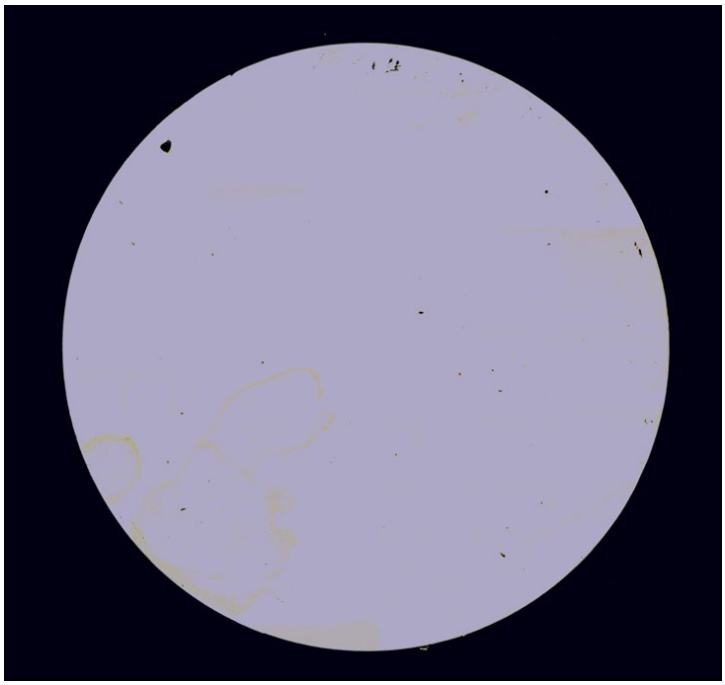

Figure 65 Resistant section of coupon 5 obtained with stitching.

6.5 Porosity

The entire resistant sections are useful for the determination of the porosity of each coupon. These photos are analyzed with ImageJ, a computer program for digital image development.

Every picture is converted to black and white, as viewed in Figure 66.

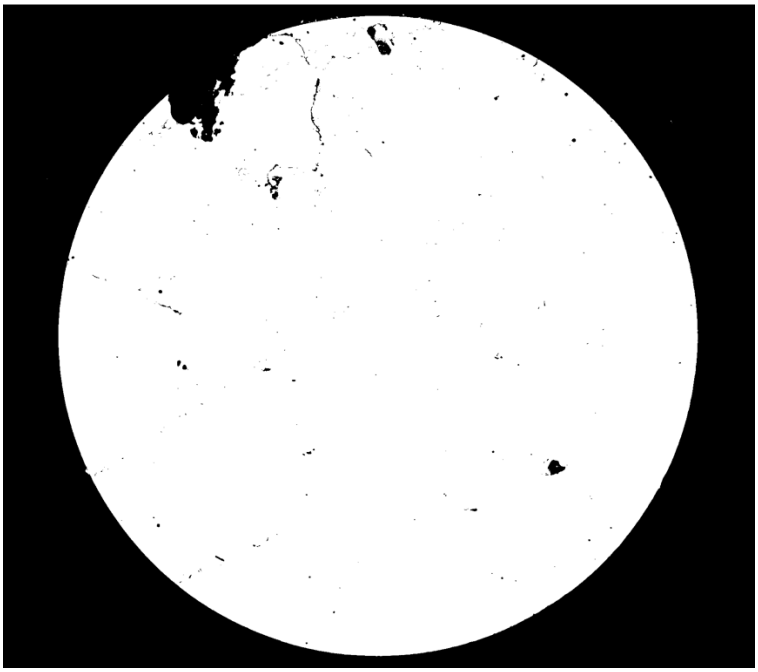

Figure 66 Resistant section of coupon 3 processed with ImageJ

A specific function gives as an outcome the % values of the white and the black areas of the resistant section. The area representative of the defects and pores is the black one. The outcomes for all the coupons are shown in Table 21.

Coupon	White area %	Black area %
3	98,599	1,401
5	99,722	0,278
6	99,616	0,384
7	99,891	0,109
11	99,917	0,083
14	99,849	0,151
15	99,377	0,623
19	99,481	0,519

Table 21 % of the white and black areas of the resistant section of coupon 3

The porosity computed can be compared with the porosity found in the static analysis presented in 3.1.6 and the relative porosity of the fatigue analysis listed in Table 11.

In the first case, the porosity is equal to 0,029% for the coupons that were printed vertically and 0,038% for the ones printed horizontally. In the second case, the relative porosity has been calculated in two different methods. For the non-heat-treated coupons the values are equal to 0,17% and 0,22%, for the heat-treated coupons the porosity values are 0,20% and 0,23% and finally, the porosity of the coupon heat-treated and machined with HIP are equal to 0,08% and 0,04%.

Some differences should be noted between these values and the porosity values listed in Table 21, related to the percentage of the black area. The porosity value of coupon 3 exhibits a huge difference from the values of the heat-treated coupons analyzed in the literature. Instead, the porosity value of coupon 11 is like the one presented in the literature. Lots of coupons show similar results to the literature ones but, the values found after the HIP process deviate a lot from the ones found experimentally.

Conformity can be found by comparing porosity values with the fatigue data. Coupon 3 was tested with a theoretical stress of 300 MPa and fulfilled a number of cycles N equal to 9696. This value of N can find an explanation looking at its porosity value, substantially higher than the values find in the literature. Coupon 19, tested with σ = 300 MPa, fulfilled a number of cycles equal to 11713, higher than coupon 3. Its porosity is lower than the porosity of coupon 3.

Similarities can be detected for coupons tested at σ = 250 MPa. Coupons related to a lower N have higher porosity values, and vice versa.

The discrepancy can be observed for the coupons tested at theoretical stresses equal to 200 MPa and 150 MPa. Coupons with higher values of porosity fulfilled a higher number of cycles during the

fatigue test. Coupons 7 and 11, tested at σ = 200 MPa, have quite similar values of porosity while coupons 14 and 15 exhibit a difference between their two porosity values.

Porosity is one of the main factors that bring the coupons to an early failure during the fatigue testing. Improving the printing of the coupons will be an advancement for gaining better fatigue behaviour.

The resistant sections of all the coupons processed with ImageJ are included in APPENDIX B.

6.6 Etching

The etching of metal surfaces allows to highlight the crystalline structure, due to the effect of selective corrosion caused by reagents on the surface areas. The proper chemical reagent and reagent application techniques are chosen by considering the material being examined.

The reagent selected is the Keller reagent and the coupons are then immersed in it for a few seconds. The etching is conducted in the Asalair Carbo 900 Chemical Suction Hood (Figure 67) with the fan and the hood active.

Coupons 14 and 15 were immersed for 20 seconds while all the other coupons were immersed for 25 seconds, and they were slightly shaken in the reagent. After the immersion, the coupons are rinsed to stop the reagent's action.

Figure 67 Asalair Carbo 900 Chemical Suction Hood

6.7 Microscope investigation of the microstructure

The coupons can be now investigated with the Nikon microscope to inspect the microstructure. The defects already presented in 6.3 and 6.4 are spotted again in the pictures taken from the microscope.

Several snaps are taken, and the resistant section can be reconstructed by stitching them together. The microstructure of coupon 3 can be seen in Figure 68.

Figure 68 Microstructure of coupon 3 observed with the microscope

The bigger irregularities identified in Figure 66 are recognized in the picture of the microstructure. In this picture, all the times in which the laser melted the powder are seen clearly.

Throughout the section, melt pools are overlaid. The overlap of the melt pools resulted from the rotation the laser performed after melting each layer.

The microstructure pictures of all the coupons are included in APPENDIX C.

6.8 Fracture surfaces

Investigations on the surfaces where the failure occurred can be done using the stereoscope, to eventually analyze any ratchet marks or crack nucleations, crack initiations or the final failure areas.

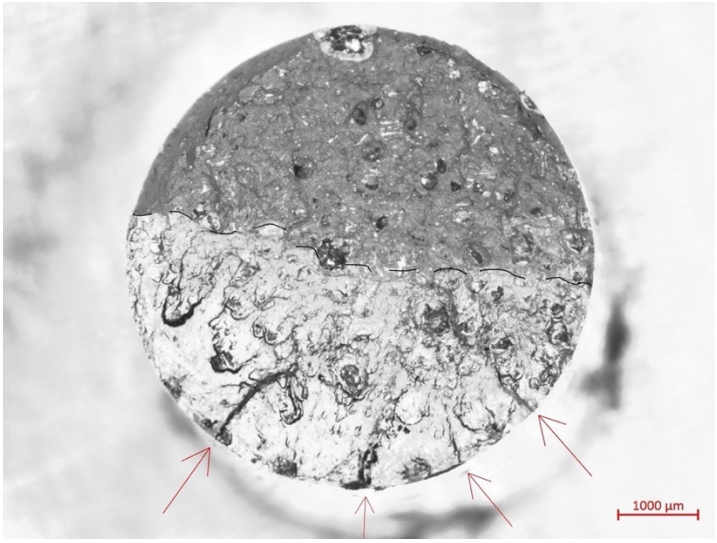

Figure 69 Fracture surface of coupon 6

The fracture surface of coupon 6 (Figure 69) has evident signs to be noted. In the final part of the section some crack nucleations have been observed (red arrows). These are strongly affected by unwanted defects like pores and occur at free surface, probably because of the less constrain by the surrounding material. The roughness, also, contributes to the crack initiation. The crack growth then is no longer affected by the material surface conditions, and it is promoted by porosity or other internal defects.

Almost half of the fracture surface is smoother than the other part, the one above the black dashed line at the centre of the section. This is the area of final fracture and is very large, indicative of the heavy load the coupon had to withstand. The final fracture area occurs when the remaining uncracked region of the cross-section is no longer able to carry the load during the fatigue cycles.

Ratchet marks are visible. There are multiple cracks joined together.

Striations are not identified in the fracture surfaces of all coupons, so no microplasticity is visible.

The fracture surface pictures of all the coupons are included in APPENDIX D.

7. Conclusions

The fatigue tests and fractography analysis of all the specimens led to a full study of the behaviour and nature of the coupons considered. The fractography in particular can help in recognizing potential errors done during the production of the coupons, to prevent repeating them.

Time is needed for the manual work involved in getting the coupons ready for metallographic and fractographic analysis. Hence, this procedure can be accelerated, and any human errors avoided by automating it as much as possible.

The results obtained in the fatigue tests are not the ones expected. When we compare them with the literature, we can observe that the values of the number of cycles obtained are lower. Therefore, the analyses can proceed by trying to identify what caused the discrepancy.

Firstly, the eccentricity values are high. This results from the additive manufacturing process which exposes the coupons to high-temperature gradients that could deform them. The high eccentricity values are a factor that weakens the fatigue behaviour of coupons.

The detailed analysis of their surface and microstructure helps in confirming that, in all probability, the printing process did not follow the right procedure. Defects have been seen both on the surface of the coupons and inside their sections, concerning porosity values that differ from the ones analyzed in the literature. This contributes to a surface finish different from the one desired.

The results of the experimental campaign differ when compared to those found in the literature. This helps in finding the mistakes committed and trying to improve the entire process.

Improvements could be made starting with the manufacturing process. Future works could try printing the coupons with different printing parameters to obtain a better surface finish and porosity and to try to avoid any deformations that could create internal stresses.

HIP (Hot Isostatic Pressing) is a technique used for reducing the porosity and increase the density of materials. The material is exposed to high temperatures and high isostatic pressures and an upgrade in the quality of the coupons analyzed can be assessed.

Another improvement could be made by adopting the Laser Shock Peening technique. It is a surface treatment where the metal surface is exposed to high-power laser pulses creating compressive shock waves. Compressive shock waves propagate into the material and generate residual compressive strains that enhance fatigue behaviour.

APPENDIX A

Grip and resistant sections observed at the microscope

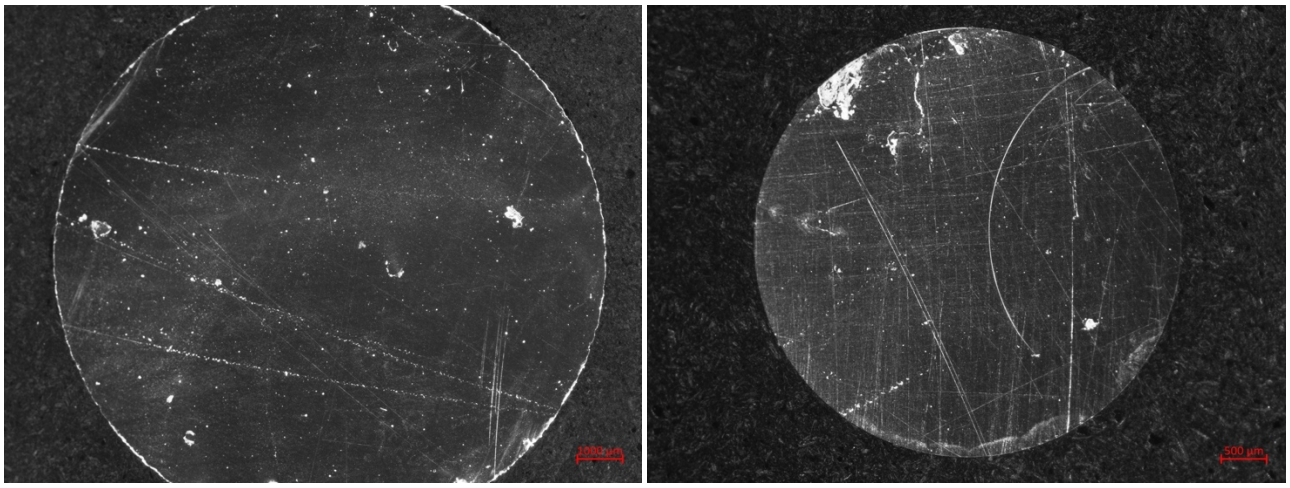

Figure 70 Coupon 3

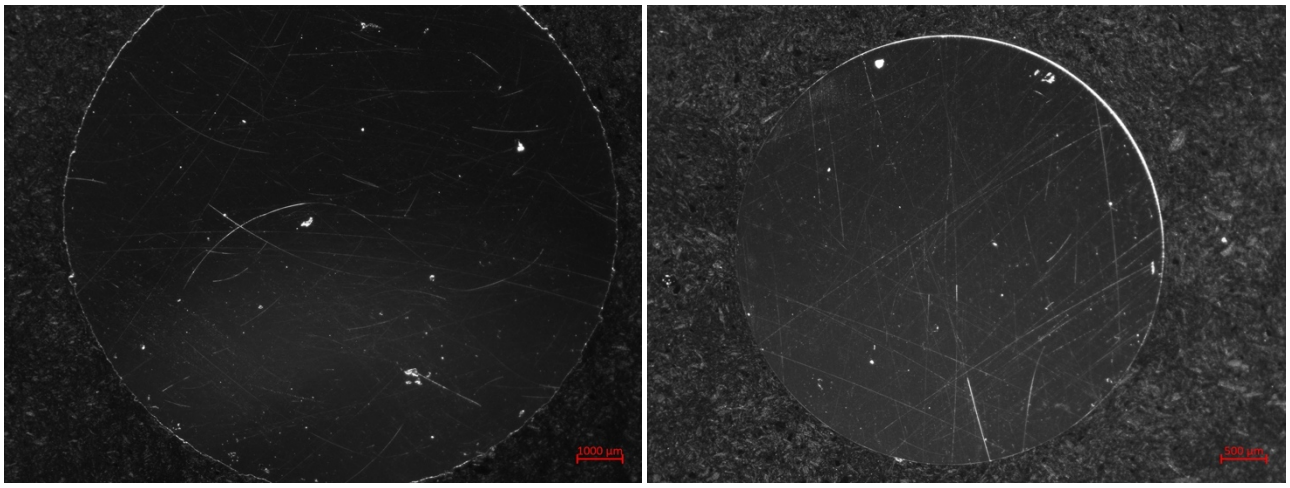

Figure 71 Coupon 5

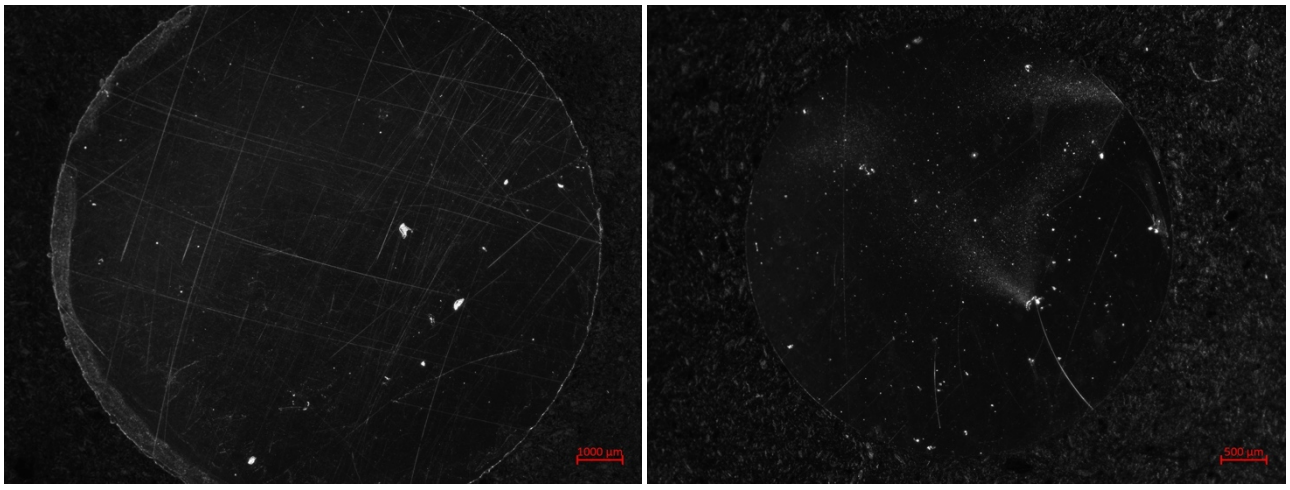

Figure 72 Coupon 6

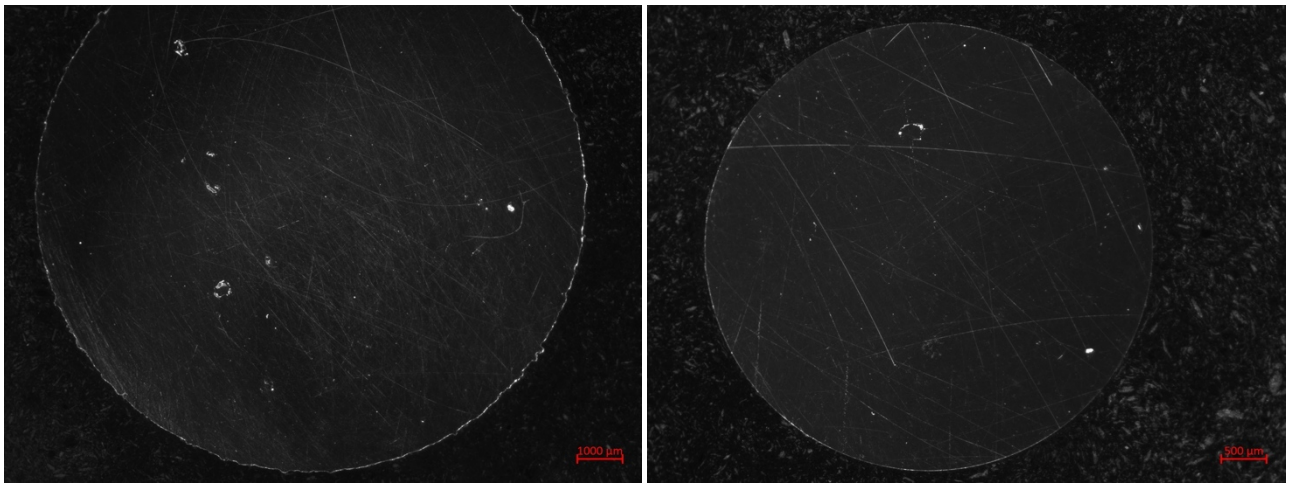

Figure 73 Coupon 7

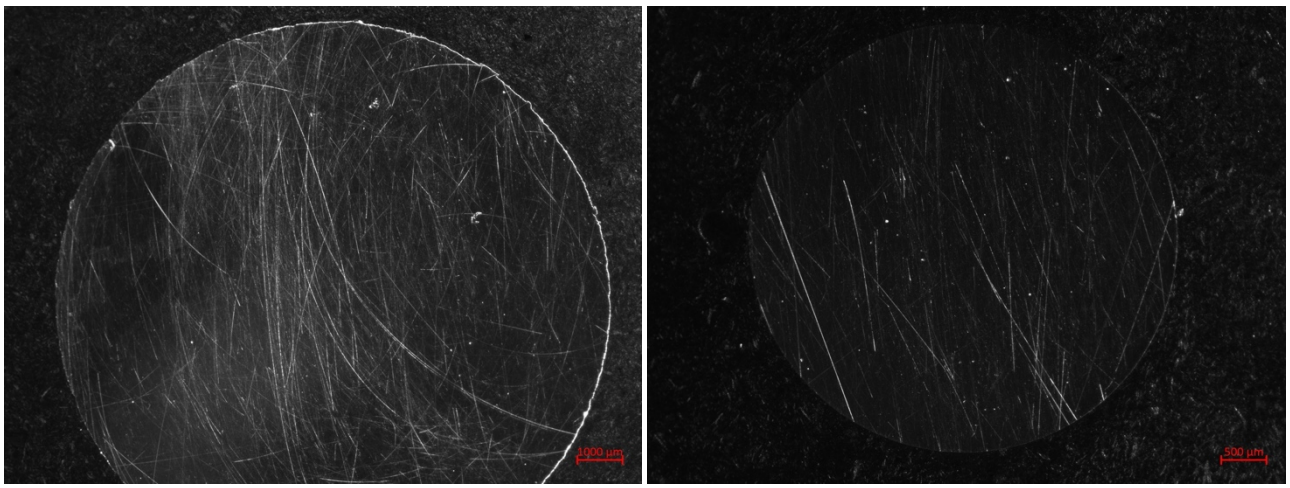

Figure 74 Coupon 11

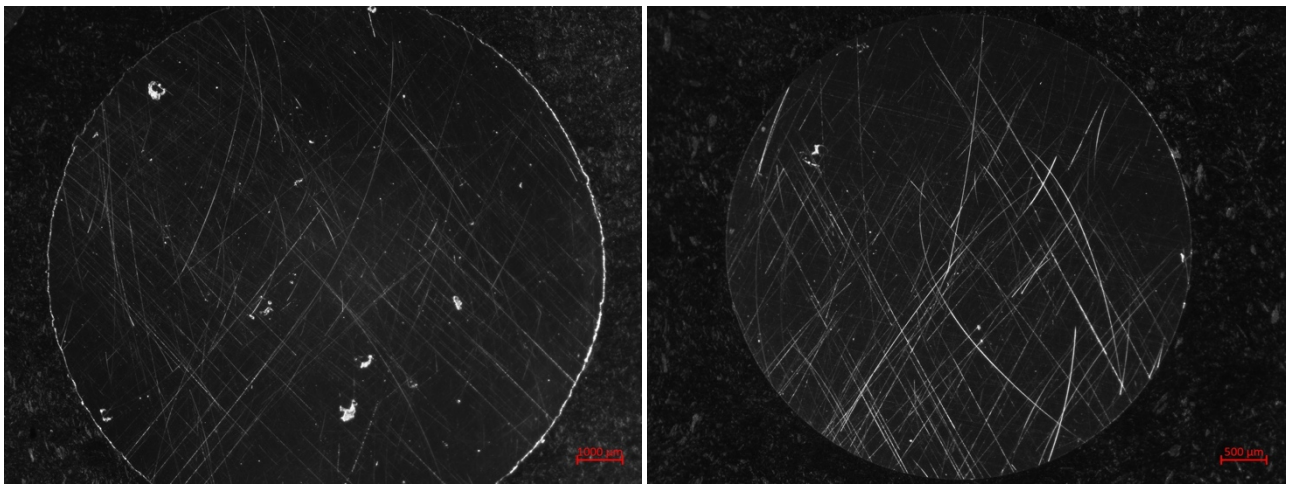

Figure 75 Coupon 14

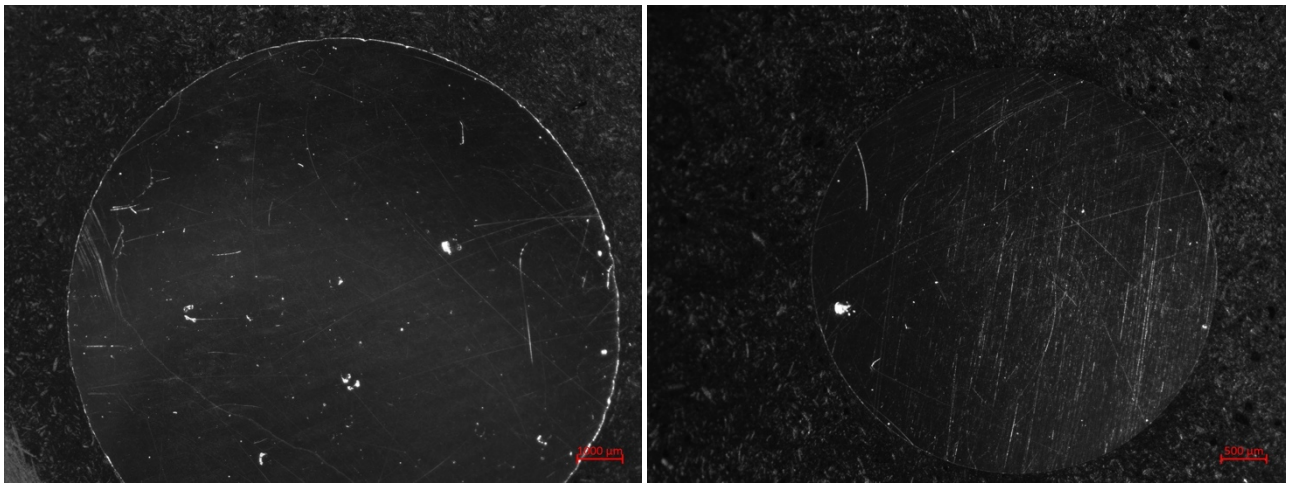

Figure 76 Coupon 15

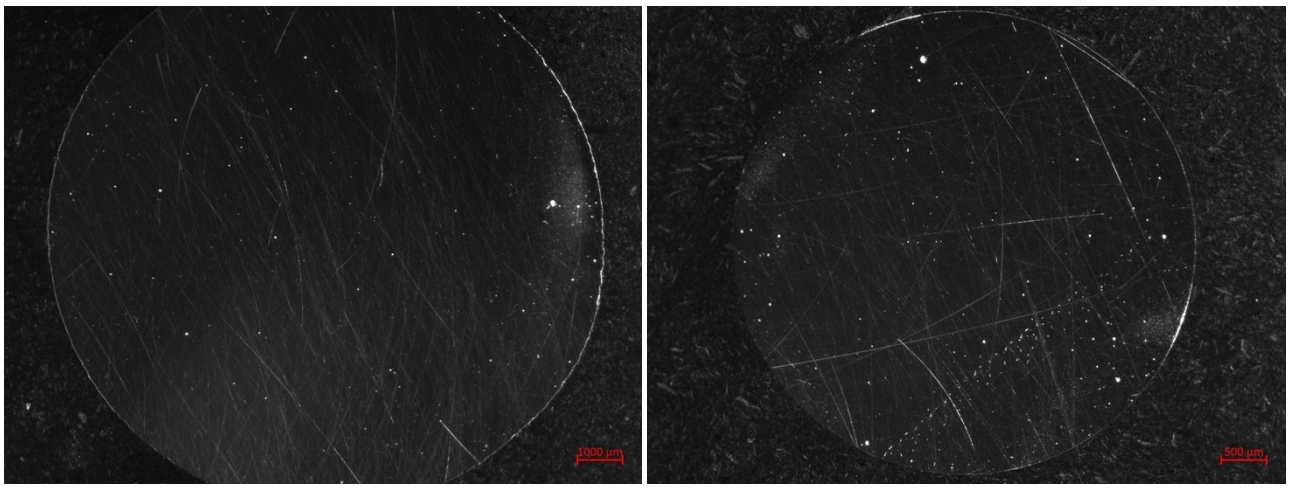

Figure 77 Coupon 19

APPENDIX B

Resistant section observed at microscope obtained from stitching photos

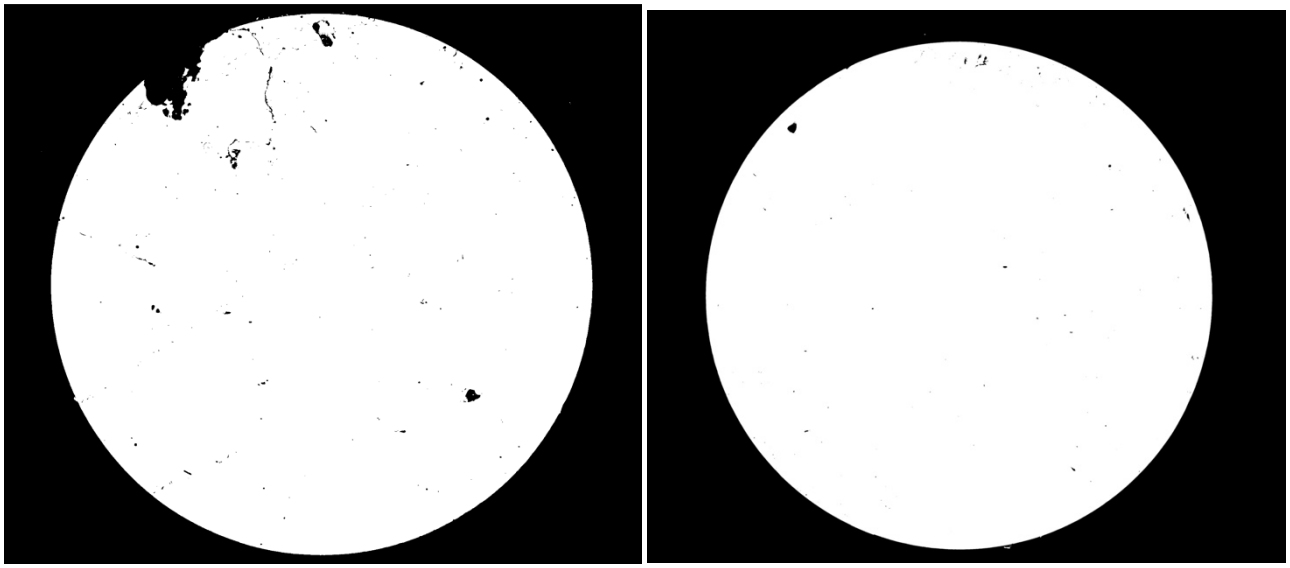

Figure 78 Resistant sections of coupons 3 (left) and 5 (right)

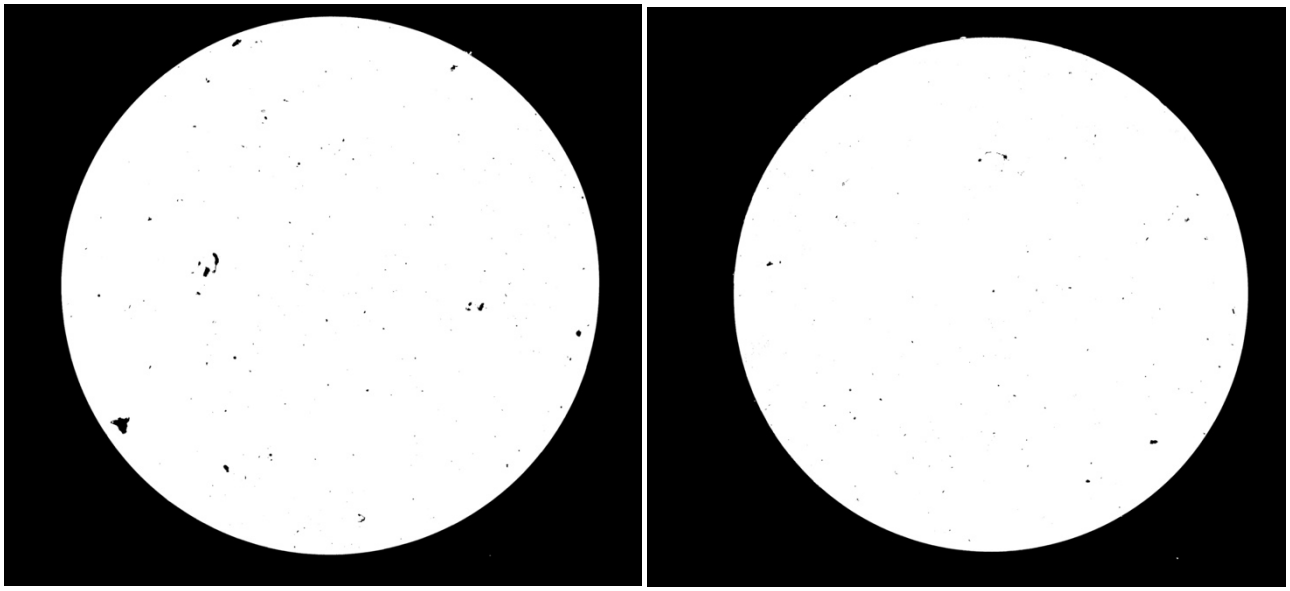

Figure 79 Resistant sections of coupons 6 (left) and 7 (right)

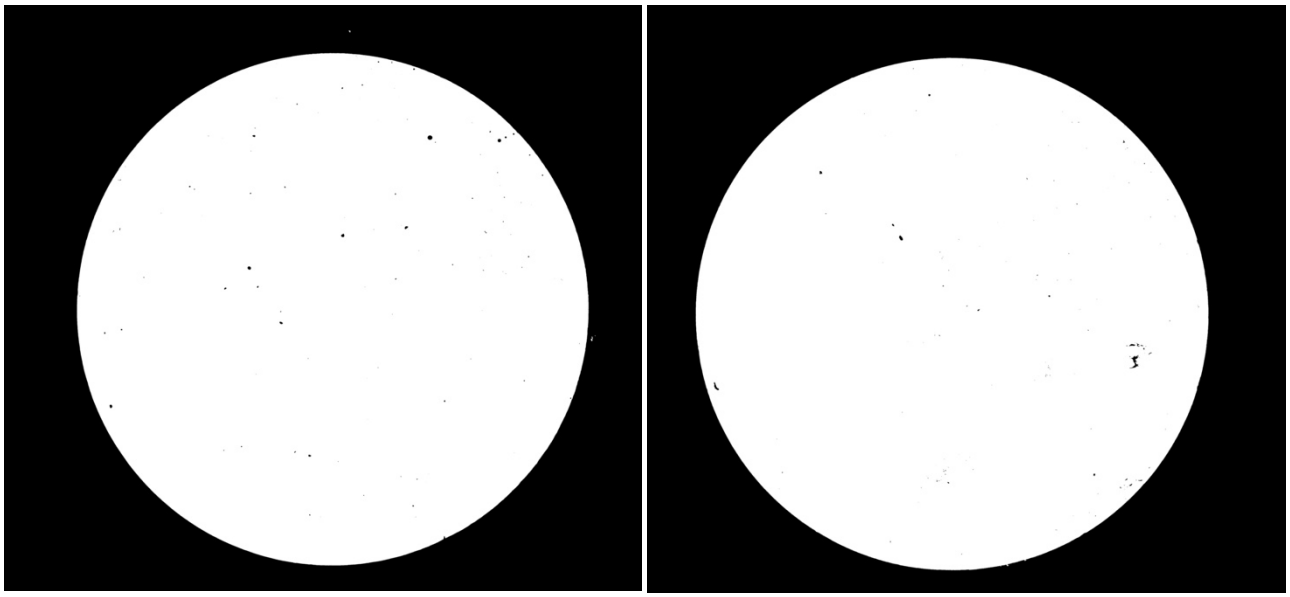

Figure 80 Resistant sections of coupons 11 (left) and 14 (right)

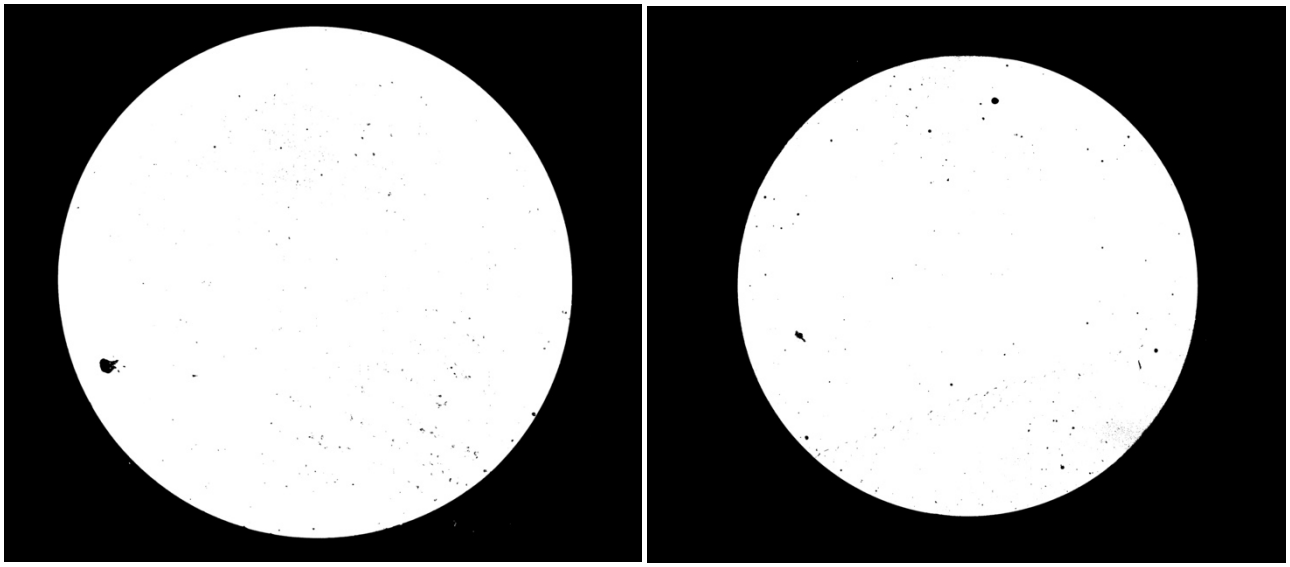

Figure 81 Resistant sections of coupons 15 (left) and 19 (right)

APPENDIX C

Microstructure of resistant sections observed at the microscope

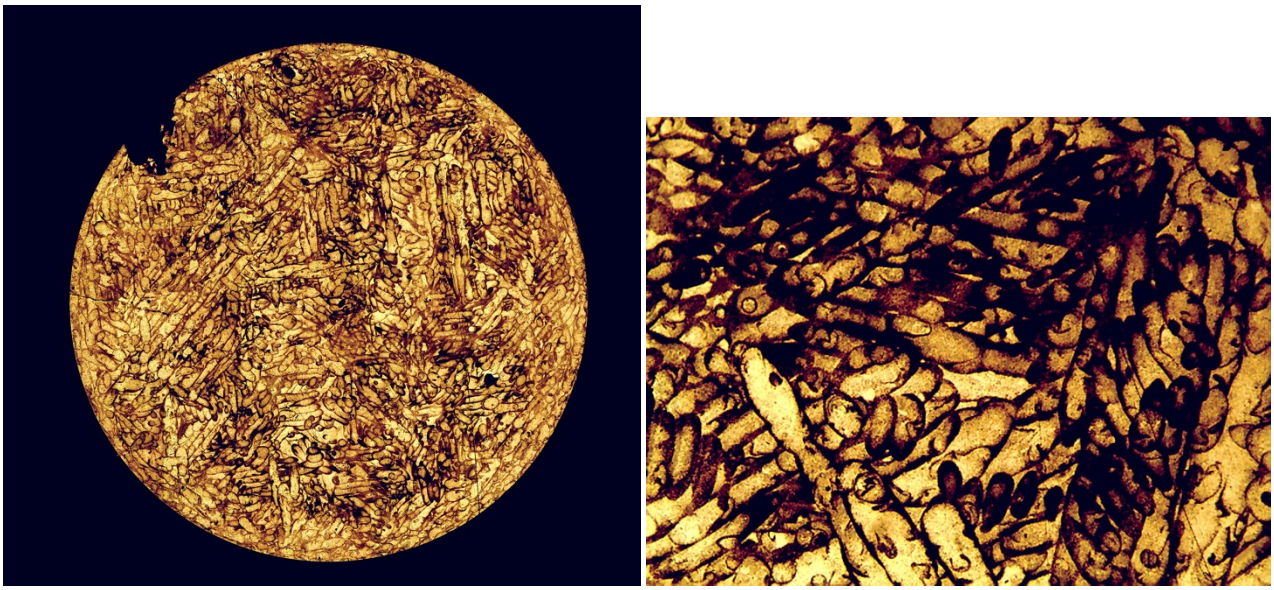

Figure 82 Microstructure of coupons 3 (left) and 5 (right)

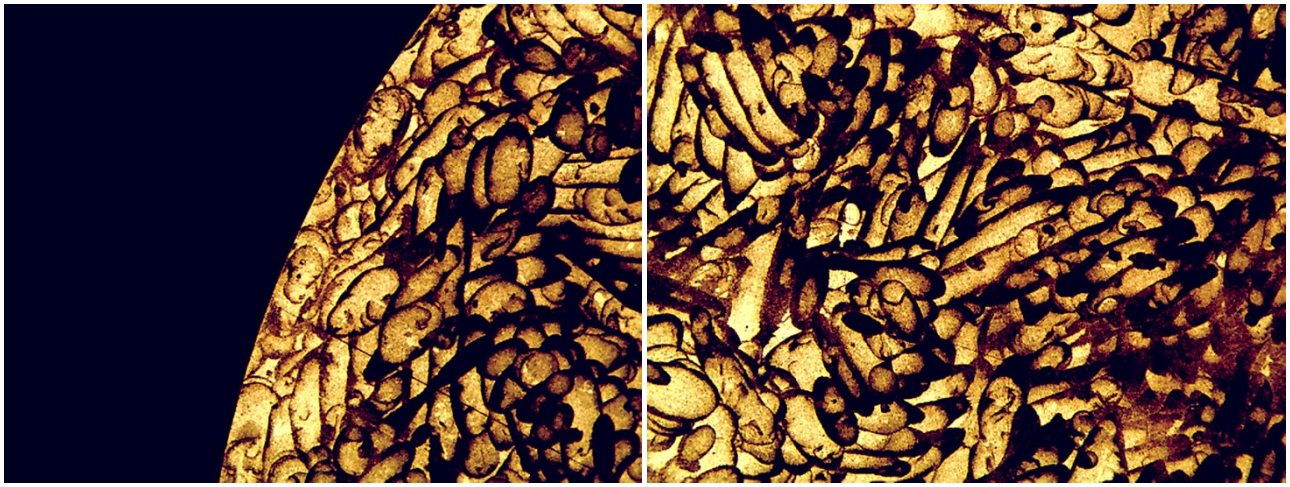

Figure 83 Microstructure of coupons 6 (left) and 7 (right)

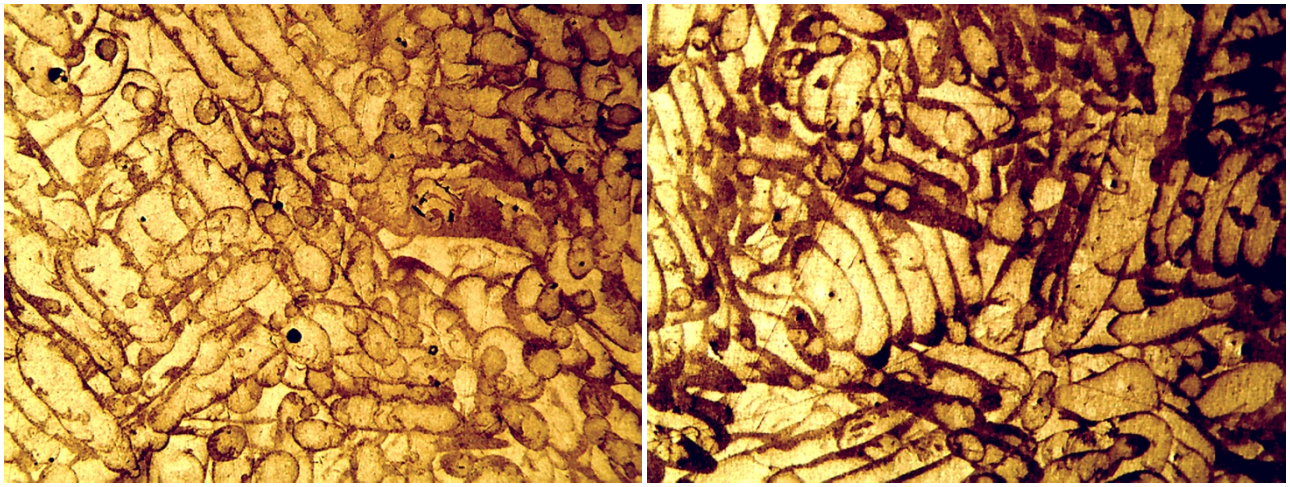

Figure 84 Microstructure of coupons 11 (left) and 14 (right)

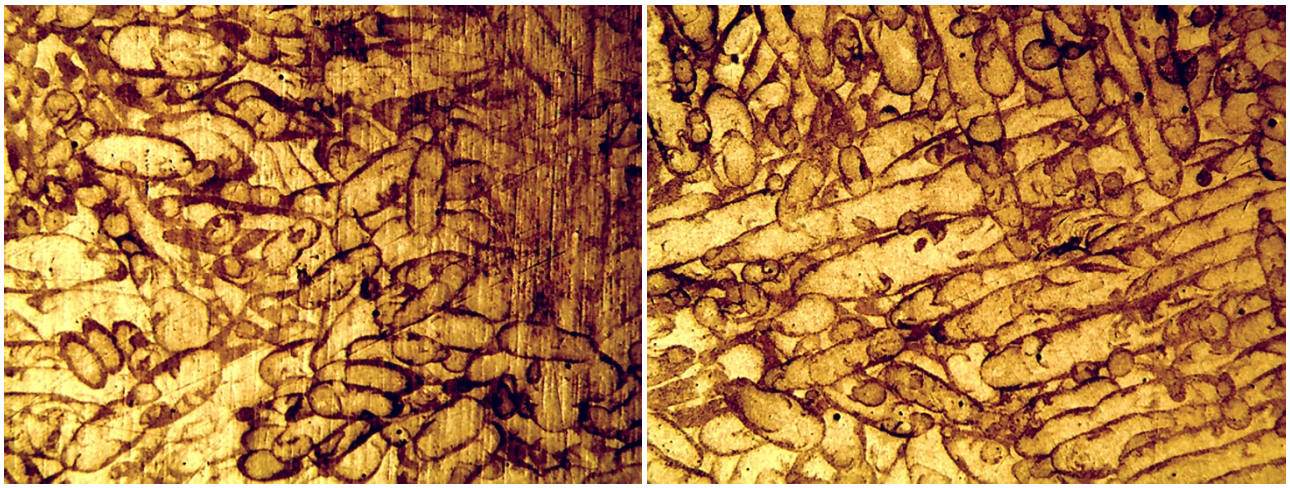

Figure 85 Microstructure of coupons 15 (left) and 19 (right)

APPENDIX D

Fracture surfaces

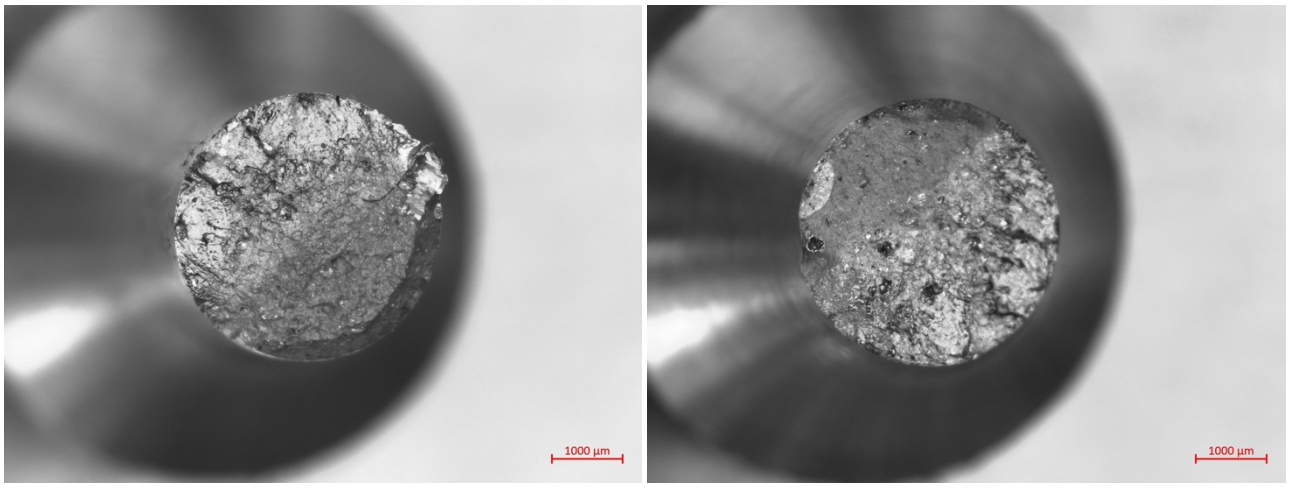

Figure 86 Fracture surfaces of coupons 3 (left) and 5 (right)

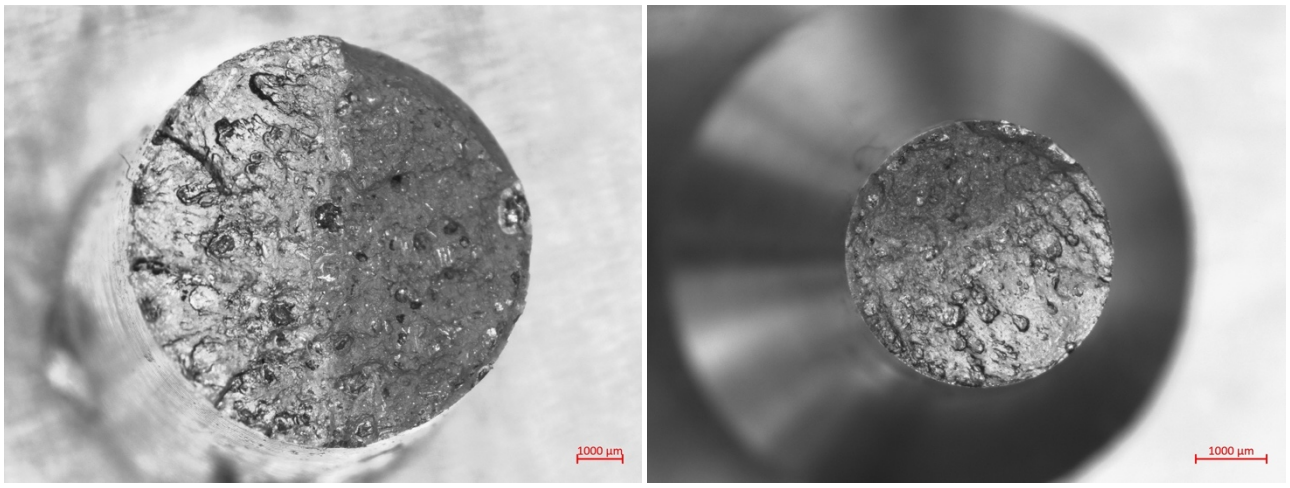

Figure 87 Fracture surfaces of coupons 6 (left) and 7 (right)

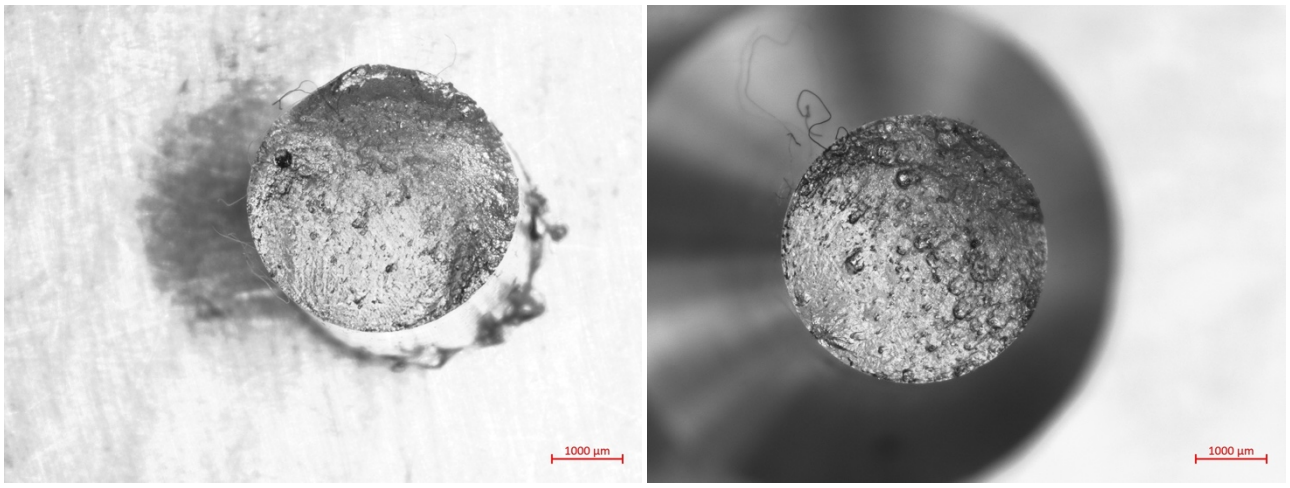

Figure 88 Fracture surfaces of coupons 11 (left) and 14 (right)

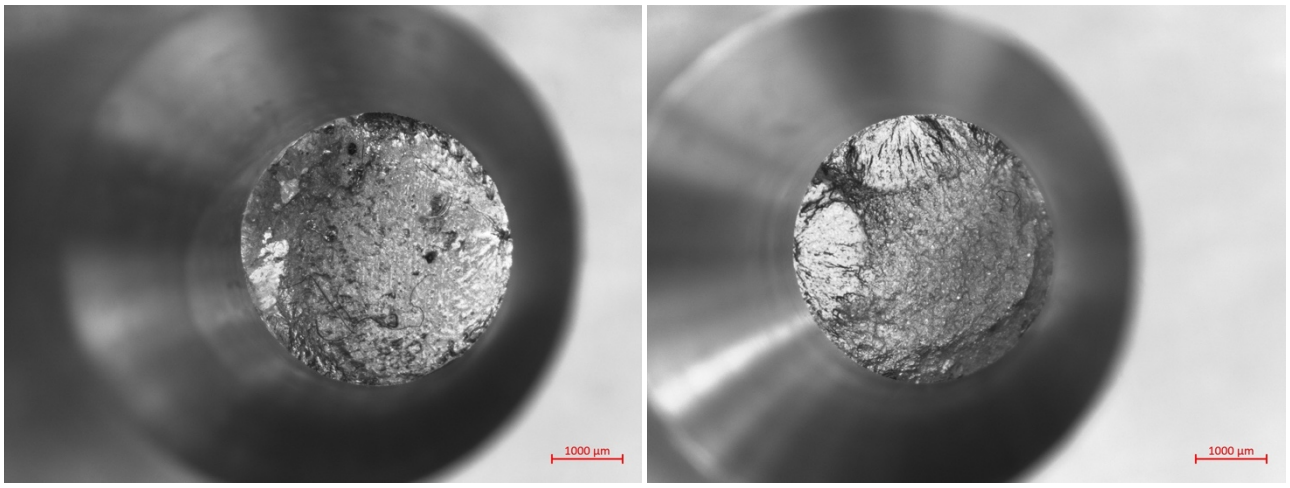

Figure 89 Fracture surfaces of coupons 15 (left) and 19 (right)

Bibliography

[1] S. Bagassi, 'Additive Manufacturing Technologies and Applications'.
[2] 'Material Selection Charts', CAD Designer & FEA Analyst. [Online]. Available: https://www.proxom.net/material-selection/
[3] I. Polmear, D. StJohn, J.-F. Nie, and M. Qian, *Light Alloys: Metallurgy of the Light Metals*. Butterworth-Heinemann, 2017.
[4] R. J. Hussey and J. Wilson, *Light Alloys: Directory and Databook*. Springer Science & Business Media, 2013.
[5] A. P. Mouritz, *Introduction to Aerospace Materials*. Elsevier, 2012.
[6] L. Donati, 'L'alluminio e le sue leghe'.
[7] 'What is Fatigue Testing?' [Online]. Available: https://www.wmtr.com/What_Is_Fatigue_Testing.html
[8] J. Schijve, *Fatigue of structures and materials*, 2. ed. [Nachdr.]. Dordrecht: Springer, 2010.
[9] A. Reyndert Christiaan, 'Fatigue and Damage Tolerance, "Phases in Fatigue Life"'.
[10] Redazione, 'La fatica nei materiali: cause e conseguenze', Vehicle CuE | Close-up Engineering. [Online]. Available: https://vehiclecue.it/la-fatica-nei-materiali-cause-e-conseguenze/10089/
[11] N. T. Goldsmith, R. J. H. Wanhill, and L. Molent, 'Quantitative fractography of fatigue and an illustrative case study', *Eng. Fail. Anal.*, vol. re, pp. 426–435, Feb. 2019, doi: 10.1016/j.engfailanal.2018.10.013.
[12] K. V. Wong and A. Hernandez, 'A Review of Additive Manufacturing', *Int. Sch. Res. Not.*, vol. 2012, p. e208760, Aug. 2012, doi: 10.5402/2012/208760.
[13] S. Alghamdi, S. John, N. Roy Choudhury, and N. Dutta, 'Additive Manufacturing of Polymer Materials: Progress, Promise and Challenges', *Polymers*, vol. 13, Feb. 2021, doi: 10.3390/polym13050753.
[14] 'The Complete Additive Manufacturing Process (Part 1) Addvance3D', Addvance3D. [Online]. Available: https://addvance3d.com/en/the-complete-additive-manufacturing-process-part-1/
[15] D. Albè, 'Definizione dei parametri di processo di una lega alluminio-scandio prodotta per Additive Manufacturing'.
[16] M. N. Cooke, 'BIODEGRADABLE BONE TISSUE SCAFFOLDS'.
[17] J. Wang, R. Zhu, Y. Liu, and L. Zhang, 'Understanding melt pool characteristics in laser powder bed fusion: An overview of single- and multi-track melt pools for process optimization', *Adv. Powder Mater.*, vol. 2, no. 4, p. 100137, Oct. 2023, doi: 10.1016/j.apmate.2023.100137.
[18] E. P. published, 'What is Selective Laser Sintering?', livescience.com. Accessed: Feb. 18, 2024. [Online]. Available: https://www.livescience.com/38862-selective-laser-sintering.html
[19] S. M. Thompson, L. Bian, N. Shamsaei, and A. Yadollahi, 'An overview of Direct Laser Deposition for additive manufacturing; Part I: Transport phenomena, modeling and diagnostics', *Addit. Manuf.*, vol. 8, pp. 36–62, Oct. 2015, doi: 10.1016/j.addma.2015.07.001.
[20] 'Binder Jetting | Additive Manufacturing Research Group | Loughborough University'. Accessed: Feb. 18, 2024. [Online]. Available: https://www.lboro.ac.uk/research/amrg/about/the7categoriesofadditivemanufacturing/binderjetting/
[21] 'Applied Sciences | Free Full-Text | Liquid for Fused Deposition Modeling Technique (L-FDM)—A Revolution in Application Chemicals to 3D Printing Technology: Color and Elements'. Accessed: Feb. 18, 2024. [Online]. Available: https://www.mdpi.com/2076-3417/13/13/7393
[22] F. Lasagni *et al.*, 'On the processability and mechanical behaviour of Al–Mg–Sc alloy for PBF-LB', *Prog. Addit. Manuf.*, vol. 7, no. 1, pp. 29–39, Feb. 2022, doi: 10.1007/s40964-021-00216-z.
[23] 'Scalmalloy Datasheet.pdf'. Accessed: Feb. 05, 2024. [Online]. Available:

https://www.carpenteradditive.com/hubfs/Resources/Data%20Sheets/Scalmalloy_Datasheet.pdf
[24] 'Microstructure and mechanical properties of as-processed scandium-modified aluminium using selective laser melting - ScienceDirect'. Accessed: Feb. 20, 2024. [Online]. Available: https://www.sciencedirect.com/science/article/pii/S0007850616300579
[25] D. Schimbäck *et al.*, 'Deformation and fatigue behaviour of additively manufactured Scalmalloy® with bimodal microstructure', *Int. J. Fatigue*, vol. 172, p. 107592, Jul. 2023, doi: 10.1016/j.ijfatigue.2023.107592.
[26] M. Muhammad, P. D. Nezhadfar, S. Thompson, A. Saharan, N. Phan, and N. Shamsaei, 'A comparative investigation on the microstructure and mechanical properties of additively manufactured aluminum alloys', *Int. J. Fatigue*, vol. 146, p. 106165, May 2021, doi: 10.1016/j.ijfatigue.2021.106165.
[27] P. D. Nezhadfar, S. Thompson, A. Saharan, N. Phan, and N. Shamsaei, 'Structural integrity of additively manufactured aluminum alloys: Effects of build orientation on microstructure, porosity, and fatigue behaviour', *Addit. Manuf.*, vol. 47, p. 102292, Nov. 2021, doi: 10.1016/j.addma.2021.102292.
[28] E. Venturi, 'Caratterizzazione di componenti in lega di alluminio Scalmalloy ottenuti per Laser Powder Bed Fusion (L-PBF)'.
[29] M. Raab and M. Bambach, 'Fatigue properties of Scalmalloy® processed by laser powder bed fusion in as-built, chemically and conventionally machined surface condition', *J. Mater. Process. Technol.*, vol. 311, p. 117811, Jan. 2023, doi: 10.1016/j.jmatprotec.2022.117811.
[30] 'Formation of precipitates and recrystallization resistance in Al–Sc–Zr alloys - ScienceDirect'. Accessed: Feb. 21, 2024. [Online]. Available: https://www.sciencedirect.com/science/article/abs/pii/S100363261161399X?via%3Dihub
[31] Y. Murakami and T. Endo, 'Effects of small defects on fatigue strength of metals', *Int. J. Fatigue*, vol. 2, no. 1, pp. 23–30, Jan. 1980, doi: 10.1016/0142-1123(80)90024-9.
[32] S. Romano, A. Brückner-Foit, A. Brandão, J. Gumpinger, T. Ghidini, and S. Beretta, 'Fatigue properties of AlSi10Mg obtained by additive manufacturing: Defect-based modelling and prediction of fatigue strength', *Eng. Fract. Mech.*, vol. 187, pp. 165–189, Jan. 2018, doi: 10.1016/j.engfracmech.2017.11.002.
[33] F. Remor, 'Study and analysis on Al-Sc alloy made by experimental tests on Al-Sc components obtained by additive manufacturing.' 2024.
[34] 'Remet, Troncatrice Tagliabarre'. Accessed: Feb. 15, 2024. [Online]. Available: https://www.remet.it/solidografia/tagliabarre.html
[35] 'Remet, Presse Inglobatrici'. Accessed: Feb. 15, 2024. [Online]. Available: https://www.remet.it/solidografia/metallografia/presse.html
[36] 'Metallographic Grinding: Grinders & Consumables :: QATM'. Accessed: Feb. 16, 2024. [Online]. Available: https://www.qatm.com/knowledge/metallographic-grinding/
[37] 'Metallographic Polishing: Polishers & Consumables :: QATM'. Accessed: Feb. 17, 2024. [Online]. Available: https://www.qatm.com/knowledge/metallographic-polishing/